

# Direct Numerical Simulations of Micro-Bubble Expansion in Gas Embolotherapy

Tao Ye

Joseph L. Bull

e-mail: joebull@umich.edu

Department of Biomedical Engineering,  
University of Michigan,  
Ann Arbor, MI 48109 USA

*We are currently developing a novel gas embolotherapy technique that involves the selective, acoustic vaporization of liquid perfluorocarbon droplets in or near a tumor as a possible treatment for cancer. The resulting bubbles can then stick within the tumor vasculature to occlude blood flow and “starve” the tumor. The potential development of high stresses during droplet vaporization is a major concern for safe implementation of this technique. No prior study, either experimentally or theoretically, addresses this important issue. In this work, the acoustic vaporization procedure of the therapy is investigated by direct numerical simulations. The nonlinear, multiphase, computational model is comprised of an ideal gas bubble surrounded by liquid inside a long tube. Convective and unsteady inertia, viscosity, and surface tension affect the bubble dynamics and are included in this model, which is solved by a novel fixed-grid, sharp-interface, moving boundary method. We assess the potential for flow-induced wall stresses to rupture the vessel or damage the endothelium during vaporization under a range of operating conditions by varying dimensionless parameters—Reynolds, Weber, and Strouhal numbers, inertial energy and initial droplet size. It is found that the wall pressure is typically highest at the start of the bubble expansion, but the maximum wall shear stress occurs at a later time. Smaller initial bubble diameters, relative to the vessel diameter, result in lower wall stresses. [DOI: 10.1115/1.1824131]*

## 1 Introduction

Embolotherapy, which involves the occlusion of vessels using foreign bodies for therapeutic reasons, is a potential means to treat a variety of cancers, such as hepatocellular carcinoma (HCC) and renal carcinoma. Currently, these methods are primarily used as a last resort when conventional therapies have failed. Although embolotherapy has only recently attracted significant interest, it dates back to 1904 when Dawbain et al. described the preoperative injection of melted paraffin-petrolatum into the carotid arteries of head and neck tumor patients [1]. In 1960, Lussenhop and Spence [2] injected spheres of methyl methacrylate into the common carotid artery of a patient suffering from an arteriovenous malformation fed by the middle cerebral artery [1]. In the 1970s, interest in embolization grew considerably due in part to improvements in catheter technology and embolic agents. These improvements in technology allowed radiologists to deliver embolic agents in a selective manner. Researchers placed silicon tubing and balloons into vessels to occlude the blood flow [3,1]. Since these early experiments, a variety of materials have been introduced through intravascular catheters and percutaneously to occlude blood flow. Some examples include absorbable materials, such as blood clot, cellulose and gelatin sponge (Gelfoam), or nonabsorbable materials, such as particulates, coils, balloons and streamers.

Boehm et al. [4] demonstrated that cancer cells can be “starved” to death by restricting blood flow to tumors. A high density of large (40–50  $\mu\text{m}$ ) solid emboli has proven effective at starving the blood supply to tissue and producing permanent tissue damage [5]. For example, HCC has been treated effectively using embolotherapy in which localized drug delivery was included in the procedure [6,1]. HCC is the most common form of liver cancer, occurring in 2–30 per 100,000 males each year, and causes an estimated 1,250,000 deaths worldwide every year. HCC has been difficult to treat with traditional methods because the

accompanying liver cirrhosis makes most patients (70–85%) ineligible for treatment by resection [6]. The results of systemic chemotherapy have been disappointing with no appreciable impact on survival rates [6]. One study indicated successful treatment by embolotherapy including 78% tumor necrosis [1], suggesting that partial necrosis is sufficient for remission. Renal carcinoma is the most common cancer in the urinary tract, accounting for ~3% of malignancies overall, and may also be well-suited for treatment by embolotherapy [1].

Most previous embolotherapy work has involved procedures that are complicated, requiring either surgical exposure of vessels near the target region or very selective catheter placement to minimize embolization of tissue collateral to the tumor. One of the major factors in the success of embolotherapy in treating tumors is the ability to direct and confine treatment to the target area. These difficulties are partially responsible for embolotherapy’s use as a last resort after conventional methods have failed.

We are developing a novel gas embolotherapy technique that is minimally invasive and provides highly selective delivery of the emboli to the tumor, minimizing the risk of damage to healthy tissue. In contrast to previous embolotherapy techniques that mainly use solid emboli, this technique uses gas bubbles, which are formed from liquid droplets, as emboli. Although the procedure has not yet been implemented in patients, current in vivo experiments have shown promise [7]. In this gas embolotherapy procedure, small (~6  $\mu\text{m}$  diameter) DDFP (dodecafluoropentane,  $\text{C}_5\text{F}_{12}$ ) droplets are first prepared in a solution of saline and albumin. The surface active albumin forms a shell around individual droplets. The droplet suspension is then injected into the vascular system at a convenient location and the droplets are subsequently transported by the blood flow. Since DDFP has a boiling point of 29°C at atmospheric pressure, the droplets of DDFP are superheated at body temperature. However, the albumin shell prevents spontaneous vaporization of the injected droplets. The droplets are imaged using standard ultrasound, and then vaporized using high

Contributed by the Bioengineering Division for publication in the JOURNAL OF BIOMECHANICAL ENGINEERING. Manuscript received by the Bioengineering Division November 6, 2003; revision received June 16, 2004. Associate Editor: Philip V. Bayly

intensity ultrasound (acoustic droplet vaporization, or ADV) at the desired location for selective delivery of emboli to the tumor. Although the droplets are small enough to pass through capillaries, the resulting bubbles are large enough to become stuck in the tumor vasculature and have a long enough lifetime,  $O(\text{days})$ , to cause infarction.

ADV is a fast process ( $< O(10^{-6})$  s) [8], and the phase change of droplets to bubbles and their subsequent rapid expansion in a confined space may potentially result in sufficiently large normal and shear stresses to rupture blood vessels and/or damage the vessel endothelium. Ultrasound-induced collapse of contrast agent micro-bubbles, a different phenomenon than ADV, has been shown to result in rupture of capillaries [9–12], which may lead to angiogenesis [13]. Neither of these is a desired effect in gas embolotherapy.

The physiological impact of the shear stresses is also a concern. The endothelium, which is the inner layer of the blood vessels, adapts to chemical and mechanical stimuli from the blood including hemodynamic shear stresses [14]. As a result, vasculature morphology [15–20], cytoskeleton organization [21–23], ion channel activation [24–26], and gene expression [27,19,28] change with the hemodynamic shear stresses. Vessel wall stress may also be relevant to the development of certain pathological conditions, including atherosclerosis [29].

In order to determine in which size vessels PFC droplets should be targeted for ADV, to determine whether smaller PFC droplets should be used, and to assess the safety risk, it is necessary to obtain detailed, quantitative information regarding the wall stresses that result from this process. While we do not foresee targeting ultrasound on specific, individual capillaries, targeting larger vessels rather than targeting entire capillary beds is an option. Although the previous work has focused on PFC droplets  $\sim 6 \mu\text{m}$  in diameter because they will pass through capillaries, the technique described above can be used to produce smaller and larger droplets.

No previous studies have reported wall stresses resulting from droplet vaporization in a tube. Given the extremely short time scale and complex dynamic characteristics of ADV, it is difficult to conduct experiments to investigate such phase change phenomena directly. The closest experiments are those reported by Kripfgans et al. [8] on a potential gas embolotherapy from an overall perspective. Although the bubbles in these experiments began as droplets, the ADV process itself was not the focus. Instead, the total bubble volume increase from the initial droplet volume was measured over a time  $\gg 10^{-6}$  s. The total volume increase includes contributions from both phase change and gas diffusion across the bubble interface. Experimental studies of micro-bubbles as contrast agents for ultrasound techniques (e.g., [30–33]) have concentrated on acoustic effects on preexisting bubbles. Other work has investigated the collapse of cavitation bubbles that were typically formed by lasers, localized heating, or flow-induced regions of low pressure. The formation of jets during the late stages of bubble collapse near a planar wall has been observed for bubbles in experimental and theoretical investigation [34,35]. Significant differences between that condition and the one reported here are that the bubble here is superheated and thus will not completely collapse, the bubbles in those studies reached sizes on the 1 mm scale, much larger than those considered here, and those bubbles were not confined in a tube. The work of Geng et al. considered the use of cavitation bubble expansion and collapse in a tube whose diameter varied between  $\sim 0.5$  and  $\sim 1$  mm for pumping [36]. None of the experiments investigated closely the ADV process and stresses on the blood vessel wall during ADV.

Theoretical studies, especially direct numerical simulations (DNS), of such problems with phase change, strong nonlinearity,

and inertia in conjunction with an unknown free interface are challenging, and the confined spatial domain inside a tube in this case compounds the complexity. The closest theoretical work is a study of bubbles as a means of pumping liquids in micro devices [37] in which it was shown that bubbles can generate appreciable flows in such devices. However, no results regarding flow stresses were reported.

The objective of the present theoretical investigation is to provide quantitative insights into the flows and stresses that result from bubble growth and collapse in a narrow, rigid tube. The simulated processes correspond to ADV and the bubble evolution that immediately follows ADV before the bubble reaches an equilibrium state.

## 2 The Computational Model

**2.1 Geometry and Assumptions.** The model geometry and computational domain are shown in Fig. 1. The expansion of a DDFP bubble in a vessel is modeled by a single, spherical bubble initially located at the center of a rigid cylindrical tube. The tube, with length,  $L$ , and inner diameter,  $D$ , is filled with an incompressible liquid, which is at rest initially. The tube opens, at both ends, to the liquid reservoir at pressure,  $P_\infty^*$ .

As reported in [8], the vaporization takes place within approximately  $10^{-9}$  s, and the phenomenon entails processes ranging across molecular, microscopic and macroscopic scales. In this investigation, a similar approach to that used by Ory et al. [37] is adopted in which the phase change process is modeled as if the droplet completely vaporizes before it expands. Immediately after the phase change, the bubble has an initially high pressure,  $P_h^* \gg P_\infty^*$ , and the same volume as the original droplet. The subsequent bubble growth and collapse processes are largely driven and controlled by this pressure and the liquid inertia. We determine the bubble evolution starting from this initial condition. At times greater than zero, the bubble pressure obeys the ideal gas law under the isothermal condition. The bubble pressure varies in response to the combined effects of liquid inertia, liquid stress, and surface tension. The process is assumed to be isothermal because bubbles originate from very small droplets whose temperatures have equilibrated with the temperature of the surrounding fluid. In summary, the present isothermal process of the inertia-driven bubble growth and collapse in a tube begins with an internal pressure of the bubble,  $P_h$ , which is much higher than the saturation pressure,  $p_v$ , i.e., the vapor pressure at the interface.

In light of the complexity of the real physical process, the work presented here is considered an initial model in our series of investigations. Future models will be extended to incorporate other significant physiological features. Some other physical mechanisms which are part of an ultrasound application involving bubbles [8], but are not vaporization related phenomena, are not included in this model. One example is the slow mass diffusion across the bubble interface after droplet vaporization. The mass diffusion is responsible for the further expansion of the bubble by influx of gases, and is also largely responsible for the eventual disappearance of the bubbles in the blood. However, it is not a phenomenon associated with the vaporization and occurs at a much slower time scale. Thus it is excluded in our computational model.

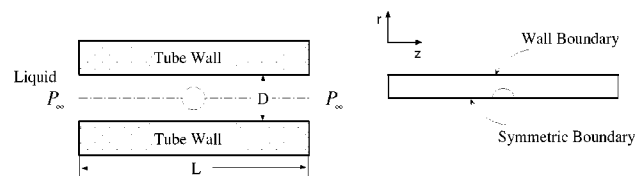


**Fig. 1 Schematic of the model geometry (left) and the computational domain (right)**

**2.2 Governing Equations.** The symbolic conventions used in the following descriptions are as follows: subscript “*l*” stands for liquid phase, “*v*” for vapor phase, “*int*” for interface, “*wall*” for wall boundary, “*n*” for normal direction at interface pointing from vapor to liquid phase, and “*r*” for reference scales used in the nondimensionalization process. We also denote dimensional variables by superscript “\*”.

The fluid dynamics of the liquid are governed by the unsteady, viscous, incompressible Navier–Stokes equations, which represent conservation of mass and Newton’s second law (momentum conservation principle) on a differential fluid element in a Eulerian framework. With constant thermodynamic and transport properties in the liquid phase, the mass and momentum conservation equations in the liquid phase can be written as

$$\nabla^* \cdot \mathbf{u}^* = 0 \quad (1)$$

$$\rho \left[ \frac{\partial \mathbf{u}^*}{\partial t^*} + \nabla^* \cdot (\mathbf{u}^* \mathbf{u}^*) \right] = -\nabla^* p^* + \nabla^* \cdot (\mu \nabla^* \mathbf{u}^*) \quad (2)$$

where  $\mathbf{u}^*$ ,  $\rho$ ,  $p^*$  and  $\mu$  are the velocity, density, pressure, and viscosity of the liquid, respectively.

The gas phase is considered inviscid and is governed by the isothermal ideal gas law:

$$P_v^* V_v^* = \text{const} \quad (3)$$

where  $P_v^*$ ,  $V_v^*$  are the pressure and the volume of the bubble, respectively. The flow is assumed to be axisymmetric and the governing equations are considered in cylindrical coordinates.

**2.3 Boundary and Interfacial Conditions.** Referring to Fig. 1, the boundary conditions specified for solving the Navier–Stokes equations are: pressure conditions at the left and right boundaries, an impermeable, fixed tube wall ( $\mathbf{u}_{wall}^* = 0$ ), and symmetry conditions for all variables at the tube centerline. At the bubble interface, mass and momentum conservation gives rise to interfacial jump conditions. For an interface moving at a velocity  $\mathbf{u}_{int}^*$ , the mass conservation condition on the interface stipulates that

$$\mathbf{u}_{int}^* \cdot \mathbf{n} = \mathbf{u}_l^* \cdot \mathbf{n} \quad (4)$$

In this study, the surface tension is assumed to be constant, so the force balance across the interface is expressed as

$$p_v^* \mathbf{n} = p_l^* \mathbf{n} - \boldsymbol{\tau}_l^* \cdot \mathbf{n} + \sigma \boldsymbol{\kappa}^* \mathbf{n} \quad (5)$$

where  $\boldsymbol{\tau}_l^*$  represents the liquid viscous stress tensor,  $\sigma$  is the surface tension, and  $\boldsymbol{\kappa}^* = \nabla^* \cdot \mathbf{n}$  is the interfacial curvature.

Note that Eq. (5) is in vector form where the liquid viscous term,  $\boldsymbol{\tau}_l^* \cdot \mathbf{n}$ , is a vector with components (zero or nonzero) in both interface normal and tangential directions. By expanding the liquid viscous term, Eq. (5) can be written as

$$p_v^* \mathbf{n} = p_l^* \mathbf{n} - [(\boldsymbol{\tau}_l^* \cdot \mathbf{n})_n \mathbf{n} + (\boldsymbol{\tau}_l^* \cdot \mathbf{n})_t \mathbf{t}] + \sigma \boldsymbol{\kappa}^* \mathbf{n} \quad (6)$$

where  $(\boldsymbol{\tau}_l^* \cdot \mathbf{n})_n$  and  $(\boldsymbol{\tau}_l^* \cdot \mathbf{n})_t$  are magnitudes in normal and tangential directions of the vector,  $\boldsymbol{\tau}_l^* \cdot \mathbf{n}$ , respectively.  $\mathbf{t}$  denotes the interfacial tangential vector.

One can decompose Eq. (6) into two component (scalar) equations. The normal component of Eq. (6), by collecting all terms in  $\mathbf{n}$ , is

$$p_l^* - p_v^* + \sigma \boldsymbol{\kappa}^* = (\boldsymbol{\tau}_l^* \cdot \mathbf{n})_n \quad (7)$$

The tangential component from Eq. (6) is

$$(\boldsymbol{\tau}_l^* \cdot \mathbf{n})_t = 0 \quad (8)$$

which is the only term remaining in the tangential direction,  $\mathbf{t}$ . If the vapor phase is viscous, there is a similar term,  $(\boldsymbol{\tau}_v^* \cdot \mathbf{n})_t$ , in the

vapor. If the surface tension is not constant, the surface tension gradient along the tangential direction,  $\partial \sigma / \partial t$ , balances the shear stress jump in the tangential stress balance. The condition of zero shear stress at the interface in the liquid follows from the inviscid (ideal gas) bubble and constant surface tension assumptions.

**2.4 Nondimensionalization.** The governing equations and boundary conditions are nondimensionalized as follows.  $L_r$ ,  $u_r$ , and  $t_r = L_r / u_r$  are the length scale, velocity scale, and time scale, respectively. The dimensionless variables are defined as  $\mathbf{x} = \mathbf{x}^* / L_r$ ,  $\mathbf{u} = \mathbf{u}^* / u_r$ ,  $t = t^* / t_r$ ,  $p = p^* / (\rho_l u_r^2)$ ,  $\rho = \rho^* / \rho_r$ ,  $\mu = \mu^* / \mu_r$ , where the liquid properties are chosen to be the reference properties, i.e.,  $\rho_r = \rho_l$ ,  $\mu_r = \mu_l$ .

The dimensionless mass and momentum conservation equations for the liquid phase are

$$\nabla \cdot \mathbf{u} = 0 \quad (9)$$

$$\text{St} \frac{\partial \mathbf{u}}{\partial t} + \nabla \cdot (\mathbf{u} \mathbf{u}) = -\nabla p + \frac{1}{\text{Re}} \nabla^2 \mathbf{u} \quad (10)$$

where

$$\text{Reynolds number } \text{Re} = \frac{\rho_l u_r L_r}{\mu_l}$$

$$\text{Strouhal number } \text{St} = \frac{L_r}{u_r t_r}$$

Note that the Reynolds number is the ratio of inertial and viscous forces, and the Strouhal number is the ratio of time dependent inertial force to convective inertial force.

The gas phase observes the ideal gas law

$$P_v V_v = \text{const} \quad (11)$$

At the bubble interface, the mass and momentum jump (balance) conditions become

$$(u_n)_{int} = (u_n)_l \quad (12)$$

and

$$p_l - p_v + \frac{1}{\text{We}} \boldsymbol{\kappa} = \frac{1}{\text{Re}} \left( \frac{\partial u_n}{\partial n} \right)_l \quad (13)$$

$$\left( \frac{\partial u_t}{\partial n} \right)_l = 0 \quad (14)$$

respectively, where

$$\text{Weber number } \text{We} = \frac{\rho_l u_r^2 L_r}{\sigma}$$

The Weber number represents the ratio of inertial force to surface tension force.

The length scale,  $L_r$ , is taken to be the tube diameter  $D$ , which is assumed to have a typical dimension of  $36 \mu\text{m}$  for arterioles. The choice of velocity scale,  $u_r$ , is less obvious as there is no apparent velocity scale in the system. The peak velocity of the interface is an appropriate velocity scale. To compute the peak velocity, which increases with initial bubble pressure, one has to integrate the interfacial acceleration, which is largely determined by the pressure, over time. This requires the knowledge of the pressure variation in time, which is part of the solution, and unknown a priori. Therefore, we estimate the peak velocity by assuming that the initial bubble pressure  $P_h^*$  is maintained invariant for a short duration  $\Delta t (= 10^{-6} \text{ s})$ , during which the two liquid columns of length  $1/2 L_t$  are pushed back by the expanding bubble, where  $L_t$  denotes the tube length. It then follows that the approximate peak velocity of the bubble interface can be calculated as

$$u_r = \frac{P_h^* - P_\infty^*}{\frac{1}{2}L_t \rho_l} \Delta t \quad (15)$$

Note that this velocity scale results in a slightly higher Reynolds number than that based on the instantaneous bubble tip velocity during the majority of the bubble lifespan. The corresponding time scale,  $t_r$ , is  $\Delta t$ .

### 3 The Numerical Method

The biofluid dynamics model outlined in Section 2 involves a deforming fluid interface. Such multiphase flows abound in applications, and pose unique challenges to the solution methods. Numerous computational approaches have been developed to deal with this type of flow. To highlight the properties required in a numerical method to solve the present problem, we briefly describe the existing methods. The boundary element method has been demonstrated to provide high accuracy for interfacial flows [38] because the governing equations are transformed to the boundaries, including the interfaces, and thus only the boundary is discretized. However, this method requires additional terms within the domain in order to consider flows which are not Stokes or potential flows [39]. Here, we only consider solution techniques for the full Navier–Stokes equations.

Two classes of methods have been used to solve interfacial flows governed by the full Navier–Stokes equations: moving-grid and fixed-grid approaches. Moving mesh/grid methods experience difficulty in handling large deformations or topological changes encountered in applications. The fixed grid methods therefore dominate recent development. Fixed-grid numerical methods include the single-domain (single-fluid) and the multiple-domain (multi-fluid) method.

The majority of current methods are single-domain methods, such as the volume of fluid (VOF) method [40], the interface-tracking/immersed boundary method [41], the level-set method [42], the phase-field [43], the ghost fluid method [44], and possibly others. Continuous and smeared interface treatment is the main characteristic of the single-domain method. The basic principle of the single-domain method is to solve one set of governing

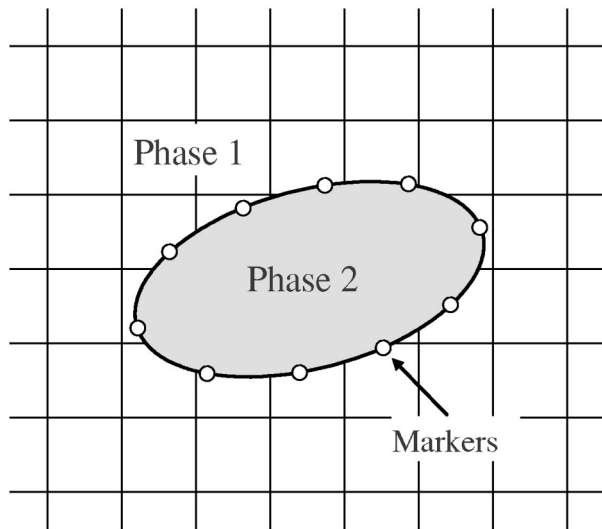


Fig. 2 Illustration of a fixed Cartesian grid and interface markers. The markers are the basic elements of the interface scheme. The interface cuts through some cells and divides the domain into two phases.

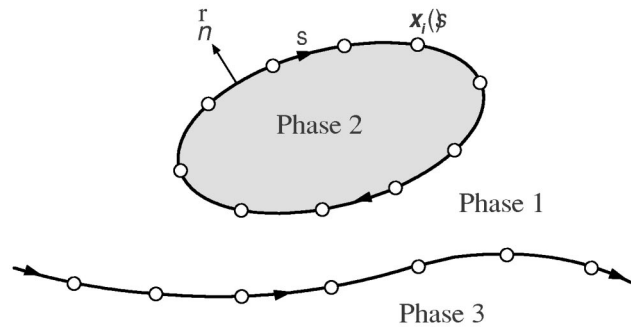


Fig. 3 Illustration of markers (empty circles), B-spline curves fitting these markers and the normal convention of the interface scheme. Here  $s$  denotes the arclength for parameterization. There can be multiple interfaces and multiple phases separated by the interfaces.

equations to account for all phases. The interfacial forces, e.g., the surface tension force, are modeled by a continuous interface technique [45] in which extra body force terms are added to the momentum equations at relevant grid cells. So the single-domain method is relatively easy to implement by extending single-phase flow methods, and has been widely used. The downside is that the field solution is continuous across different phases in the domain. Consequently, the order of accuracy of the overall solution is reduced to first-order or even lower [46]. This is the continuous aspect of the single-domain method. The extra body force terms in

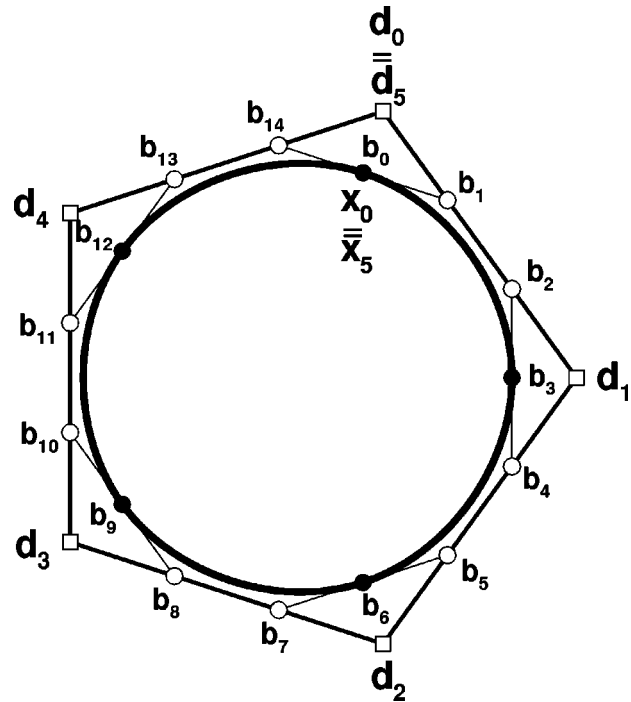
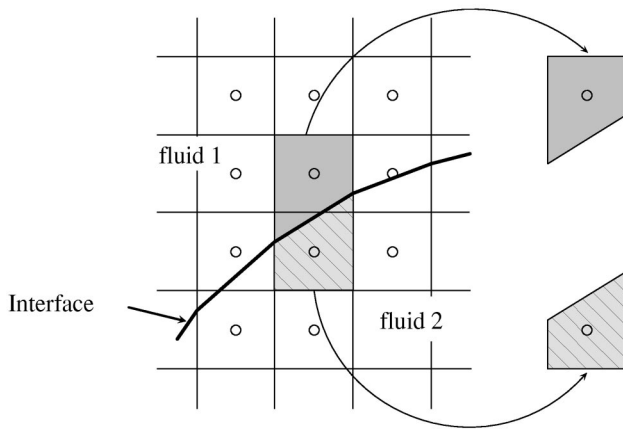


Fig. 4 An illustration of finding a  $C^2$  cubic B-spline interpolatory curve (inner circle in thicker line), given, say, 5 points  $X_i$  (solid circles). Here  $X_i$  are interfacial markers to be fitted by the B-spline curve. B-spline control polygon  $d_i$  (empty squares) and Bézier control polygon  $b_i$  (empty circles) are necessary intermediate points to generate the final B-spline curve. Between any two points  $X_i$  (solid circles), there is a piece-wise Bézier curve (thicker line), which is a cubic polynomial curve.  $C^2$  means these piece-wise Bézier curves are continuous up to second derivatives at their junction points,  $X_i$ . See Farin [50] for details of the algorithm.



**Fig. 5** Illustration of an interface, an underlying fixed grid, cut cells and reshaping of cut-cells to form trapezoidal cells (shaded). Notice that two fluids are separated by the interface. The trapezoidal cells conform to the interface for a sharp interface treatment.

the single-domain method are added at a band of grid cells enclosing the interface. The effect of the interface is smeared over several grids. The “smearing” is required in order to alleviate the numerical stiffness associated with large property ratios across the interface. Adding the extra body force terms within a band of grid cells constitutes a finite-thickness interface treatment. This is the “smearing” aspect of the single-domain method. Because of the continuous nature of the single-domain method that resulted from solving a single set of equations, it is not trivial to specify different models for liquid and vapor phases in different regions of the computational domain. That poses challenges to the present model involving an ideal gas model in vapor phase. More importantly, the pressure difference across the capillary interface is smoothed/diffused by the continuous interface treatment of the single-domain method [47] because of continuous and smearing nature of the method. In this case, the single-domain method would underestimate the liquid pressure due to excessive numerical diffusion, yielding a lower wall pressure. However, an accurate prediction of the wall stresses is critical in our investigation. Therefore, the single-domain method is not suitable for the present study.

The multi-domain, or otherwise known as cut-cell, method overcomes these drawbacks, and treats any type of interface as sharp (as opposed to smeared) and discontinuous (as opposed to continuous). In the multi-domain method, interfaces, typically represented by polynomial or spline curves (surfaces in 3-D), intersect with the grid and split the computational domain into multiple subdomains. Each subdomain represents one phase/material. Mathematical models can be specified separately for each phase/material. Multiple sets of governing equations are solved as opposed to one set in the single-domain method to maintain the discontinuity of the solution and eliminate the source of the erroneous diffusion. Moreover, cut cells are reshaped to conform to the interface to enable sharp interface treatment. The boundary conditions on the internal interfaces, such as stress conditions for fluid-fluid interfaces, are applied at the interfaces directly instead of on the underlying grid. The use of multi-domain, sharp-interface methods is rare in part because of implementation challenges and higher computational cost.

In this work, we employed a multi-domain, sharp-interface method [48,49,47] that allows us simulate flows with moving interfaces on fixed Cartesian grids. The need for an accurate treatment of the interface in order to obtain accurate wall stresses necessitates the use of this approach.

### 3.1 Overview of Multi-Domain, Sharp-Interface Method.

The current combined Eulerian–Lagrangian method consists of a

fixed Eulerian grid, and Lagrangian geometric entities representing the interfaces as illustrated in Fig. 2. The field solution is obtained on an underlying fixed grid while the interfaces are explicitly tracked by B-spline curve schemes. To deal with the non-linear coupling between the Eulerian (field solution) and Lagrangian (interfaces) elements, an implicit, iterative procedure is used. The present method has second-order accuracy in computing various flows with embedded interfaces or boundaries [48,49,47].

### 3.2 Interface Scheme and Curvature Calculation.

The interface is explicitly tracked using Lagrangian marker points. From these markers, we can determine the shape and location of the interface, and its curvature and other geometric parameters, eliminating possible ambiguity in estimating the interface otherwise. The movement of the interface on the fixed Eulerian grid is determined by the kinematic or dynamic conditions. This method can be applied to fixed solid boundaries with irregular shapes [48] or moving phase boundaries [49] (see Fig. 3).

A  $C^2$  cubic B-spline curve, which is a composite curve comprised of piecewise cubic Bézier curves joined at the marker points, interpolates a set of marker points [50] to construct the interfaces.  $C^2$  denotes the degree of the smoothness of the composite B-spline curve, where the superscript “2” in this case indicates that any two neighboring Bézier curves have equal second derivatives about the parametrization at their joint. In other words, the B-spline curve is continuous in zeroth (curve itself), first and second derivatives at any marker (Fig. 4). Since each Bézier curve segment is defined by only four markers, the composite B-spline curve can fit complex (with large curvature variations) shapes supported by the entire set of markers. The translation and deformation of the interface is accomplished through the motion of individual marker points, which is determined by the interfacial boundary conditions computed from flow quantities on the underlying fixed grid.

The curvature, which involves second-derivatives of the interface parametrization, is commonly known to suffer severely from spurious oscillations as a result of finite-precision floating-arithmetic on digital computers [50]. It is true even with a  $C^2$  B-spline curve interpolation. In continuum interface methods, the excessive diffusion, albeit detrimental to accuracy, helps to dampen out the numerical noises in the curvature profile. However, sharp interface methods eliminate erroneous numerical diffusion, leaving numerical stability of the solution process prone to noises in the curvature profile. Our solution is to use a fairing algorithm to obtain an accurate and smooth curvature profile [51,50] without compromising the benefits derived from our method. The curve smoothing is analogous to high wave number noise filtering in the frequency domain using signal processing. For the lower wave number, real signals are retained. The filtering is required because (1) numerical noise (roundoff error) is inevitable in computer simulations, and (2) the curvature involves second derivatives about the parametrization (coordinates). There are two ways to cope with the noise associated with the interface tracking: spectral and geometrical smoothing. In our method, we use a geometrical fairing algorithm that operates on the curve itself to reduce the noise in the computed curvature. The “fairing” algorithm makes the piece-wise curve three-times differentiable at the problematic marker points by adjusting the corresponding vertex of the spline control polygon. The resulting correction (in terms of changes in coordinates of the marker points) of the smoothing algorithm to the curve is negligibly small so that curve itself does not have perceivable differences before and after fairing. Such correction in a fairing procedure to a randomly chosen curve is examined and plotted in [49]. This approach is widely used in engineering design of perfect curves, and it ensures that the smoothing of the curvature does not alter the geometry. Pure spectral filtering is subject to the disassociation of the curvature

**Table 1 Summary of dimensionless parameters used in the simulations**

Case	Re	We	St	Initial pressure $P_h$	Initial diameter $d_i$
1	427.59	6.93	10.47	176.39 ( $P_h^* = 20$ bar)	0.1
2	106.90	6.93	10.47	176.39 ( $P_h^* = 20$ bar)	0.1
3	427.59	3.46	10.47	176.39 ( $P_h^* = 20$ bar)	0.1
4	202.39	1.55	22.11	393.66 ( $P_h^* = 10$ bar)	0.1
1-1	427.59	6.93	10.47	176.39 ( $P_h^* = 20$ bar)	0.3
1-2	427.59	6.93	10.47	176.39 ( $P_h^* = 20$ bar)	0.5
1-3	427.59	6.93	10.47	176.39 ( $P_h^* = 20$ bar)	0.7
1-4	427.59	6.93	10.47	176.39 ( $P_h^* = 20$ bar)	0.9

from the underlying geometry (such as normal and tangent of the curve), a probable accuracy degradation warranting further examination.

**3.3 Cartesian Grid Method for Flows With Fixed Interfaces.** Unlike a usual body-fitted grid method for flows with embedded interfaces, in our fixed Cartesian grid method, the grid lines do not conform to the interfaces, eliminating the need to regenerate the grid as the bubble interface evolves. To solve the flow field, one needs to discretize equations on cells cut by the interfaces and to specify the boundary conditions at the interfaces. We employ a merged cut-cell approach. That is, the cells cut by the interface are split into two parts: the partial cell containing the center of the original Cartesian cell and maintaining the initial cell index, and the remaining portion merged with a neighboring cell belonging to the same phase. As illustrated in Fig. 5, this procedure results in irregular and trapezoidal shaped cells around the interfaces. Away from the interfaces, computational cells are structured and Cartesian. In this algorithm, the nominal structured grid index system is maintained. A special interpolation scheme is devised to discretize the reshaped cut-cells to second-order accuracy. To impose boundary conditions, we employ an extrapolation algorithm at the interfaces.

Interfaces cut the computational domain into multiple subdomains that represent different phases/materials. Each subdomain is coupled with the neighboring subdomains via interfacial boundary conditions. Because of the merging practice, the current method does not result in small cells, thus is free from the problems associated with small cells, a typical issue of other cut cell methods. For example, the normalized cell sizes of the entire computational domain range from 0.5 to 1.5 for a uniform grid in the present method.

In the liquid phase, a finite volume, fractional step method [52–54] is employed to solve the Navier–Stokes equations. The discretization procedure deals with both Cartesian and trapezoidal cells. The reshaping procedure maintains flux conservation around

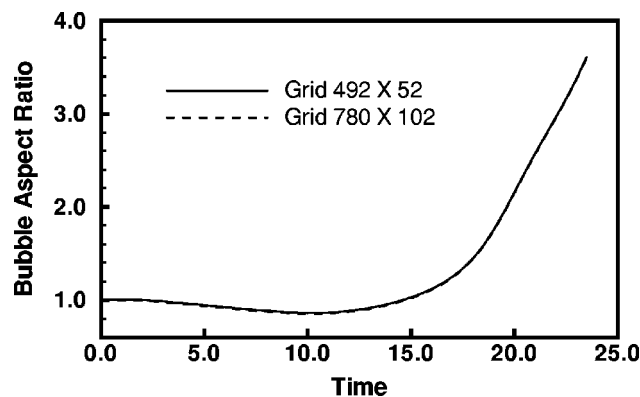


**Fig. 6 History of the bubble aspect ratio obtained on two different grids for case 1 in Table 1. It confirms the grid chosen has sufficient resolution.**

the interface, so the conservation laws (mass and momentum) are honored at all resolvable scales, including those computational cells intersecting with phase boundaries. Consistent interpolation formulas are used to compute the fluxes along any of the cell surfaces including a linear-quadratic interpolation to handle the non-Cartesian cell faces [48,49]. Both inviscid and viscous terms are discretized so as to create a globally second-order accurate algorithm. For time-integration (of the unsteady term) in the Navier–Stokes equations, the convective terms are treated explicitly using a second-order Adams–Bashforth scheme, and the viscous terms are treated semi-implicitly with a Crank–Nicholson scheme. An algebraic multigrid solver is employed to solve the discretized pressure Poisson equation. Since the stencil on those grid cells cut by the interface is slightly larger than the standard five-point stencil, the algebraic multigrid method avoids the difficulties encountered by the geometric multigrid method in unstructured geometry. The computational code is parallelized using OpenMP.

**3.4 Iterative Algorithm for Flows With Moving Interfaces.** For flow problems subject to moving interfaces/boundaries, we need to solve the system within each time step such that, simultaneously, the flow field satisfies the Navier–Stokes equations (9) and (10), and interfacial conditions (12) and (13) are enforced at the interface. During this procedure, the interface location has to be obtained as part of the solution. Solution of the Navier–Stokes equations is a boundary-value problem on a domain bounded by the gas-liquid interface which moves and deforms because of the flow. This gives rise to a nonlinear coupling between the flow field and the interface. One way to deal with this nonlinear coupling is to use a prediction-correction type iterative procedure. The implicit iterative algorithm to solve for flow fields and interfaces using the normal stress boundary condition within each time step is outlined by the following steps.

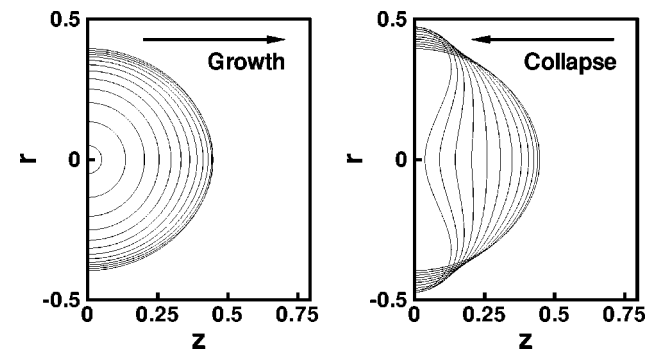


**Fig. 7 Bubble shapes at different times during growth (left graph) and collapse (right graph) for case 1 in Table 1,  $Re = 427.59$ ,  $We = 6.93$ ,  $St = 10.47$ ,  $P_h = 176.39$  ( $P_h^* = 20$  bar),  $d_i = 0.1$ . Only half of the bubble is shown because of the symmetry. Time interval between successive shapes is 1 dimensionless unit ( $10.5 \times 10^{-6}$  s/unit). The computational domain extends to 16 in both directions on the z axis.**

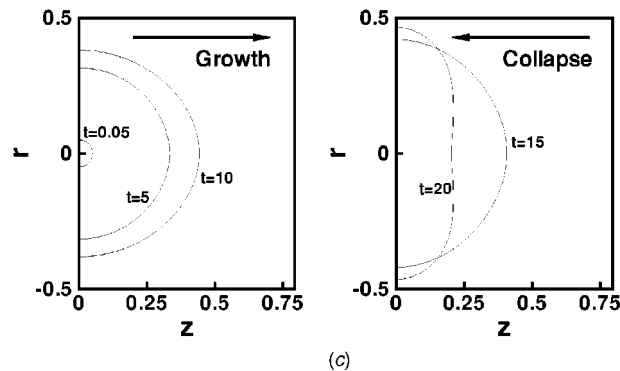
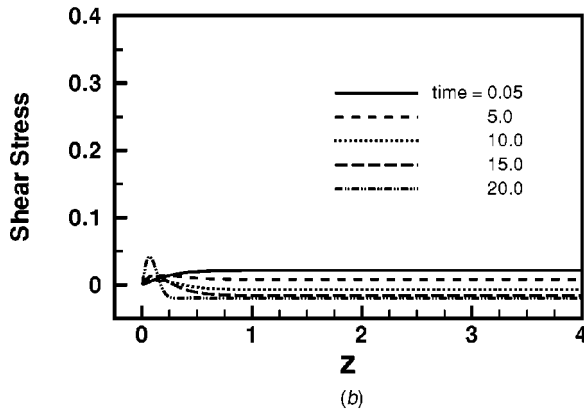
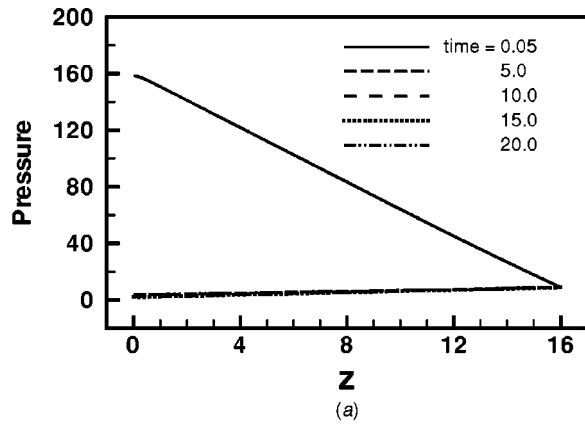


**Fig. 8** (a) Pressure and (b) shear stress along the top wall of the tube at various times for case 1 in Table 1,  $Re=427.59$ ,  $We=6.93$ ,  $St=10.47$ ,  $P_h=176.39$  ( $P_h^*=20$  bar),  $d_i=0.1$ . The horizontal axis indicates axial position,  $z$ . Only the significant portion of the tube,  $z \leq 4$ , for shear stress is shown. The dimensional stress is  $11,338.8$  N/m<sup>2</sup> per dimensionless unit. (c) Bubble shapes at times presented in (a) and (b).

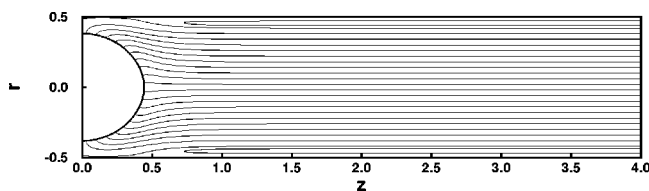


**Fig. 9** Streamline plot at  $t=10$  for case 1 in Table 1,  $Re=427.59$ ,  $We=6.93$ ,  $St=10.47$ ,  $P_h=176.39$  ( $P_h^*=20$  bar),  $d_i=0.1$ . Half of the domain is shown.

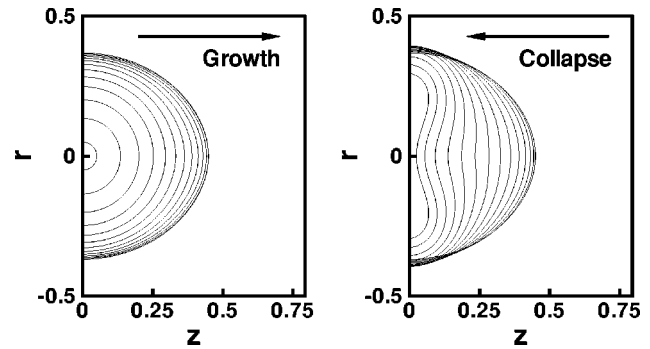


**Fig. 10** Bubble shapes at different times during growth (left graph) and collapse (right graph) for case 2 in Table 1,  $Re=106.90$ ,  $We=6.93$ ,  $St=10.47$ ,  $P_h=176.39$  ( $P_h^*=20$  bar),  $d_i=0.1$ . Only half of the bubble is shown because of symmetry. Time interval between successive shapes is 1 dimensionless unit ( $10.5 \times 10^{-6}$  s/unit). The computational domain extends to 16 in both directions on the  $z$  axis.

1. For a given shape of the bubble, the flow field is first computed by solving the Navier–Stokes equations. During this step, only a small number of iterations on the pressure Poisson equation are needed. At the first iteration of current time step, the bubble shape is obtained from last time step.
2. After the flow field is solved, the normal stress boundary condition at the interface, Eq. (13), is checked. If it is not satisfied, the interface shape is corrected based on the residual of Eq. (13):

$$\mathbf{x}_{int}^{n,k+1} = \mathbf{x}_{int}^{n,k} + \beta \left( \tau_n - \frac{1}{We} \kappa \right) \mathbf{n}$$

where  $\mathbf{x}$  stands for the interfacial marker location,  $n$  for time step,  $k$  for the inner iteration count within a time step,  $\mathbf{n}$  for normal direction.  $(\tau_n - (1/We)\kappa)$  is the residual form of Eq. (13) by moving all terms to the right hand side of the “=” sign, with  $\tau_n$  representing all terms except the capillary term.  $\beta$  is the under-relaxation factor used in the computation, whose optimal value depends on the problem and is typically in the range of  $10^{-6}$ – $10^{-2}$  in our simulations.

After each interface updating step, the mass conservation is checked. If it is not satisfied, it is enforced by a rescaling procedure, as detailed in [49].

If all equations and boundary conditions are satisfied within roundoff tolerances, the iteration of this time step is completed and the computations move on to next time step to repeat the process.

## 4 Results and Discussion

Convective and time-dependent inertia, viscosity, surface tension, initial bubble pressure and initial bubble size play central roles in the resulting bubble dynamics. Their relative importance is indicated by the following dimensionless parameters: Reynolds number, Weber number, Strouhal number, initial bubble pressure, and initial bubble size. We examined the effects of these parameters on the wall stress conditions.

The computed cases are summarized in Table 1. The cases are organized according to the initial bubble diameter,  $d_i$ . Cases 1–4 all have an initial bubble diameter of  $d_i=0.1$  but with different liquid viscosity, surface tension or initial bubble pressure. Case 2 differs from case 1 with a higher liquid viscosity; case 3 has a higher surface tension coefficient than 1; case 4 represents the case with a lower initial pressure,  $P_h^*=10$  bar, which results in the variations in other dimensionless parameters as well. Cases 1-1, 1-2, 1-3, and 1-4 have the same dimensionless parameters of case 1 except the bubble diameter.

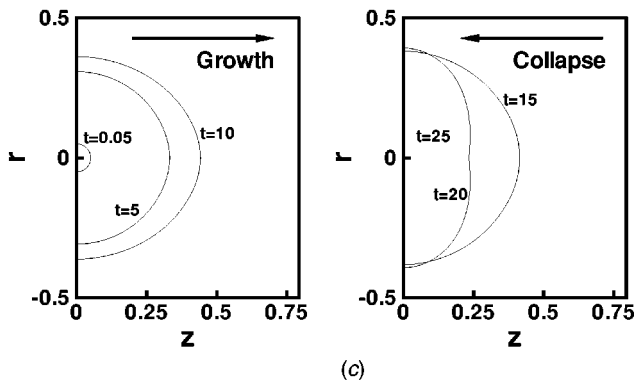
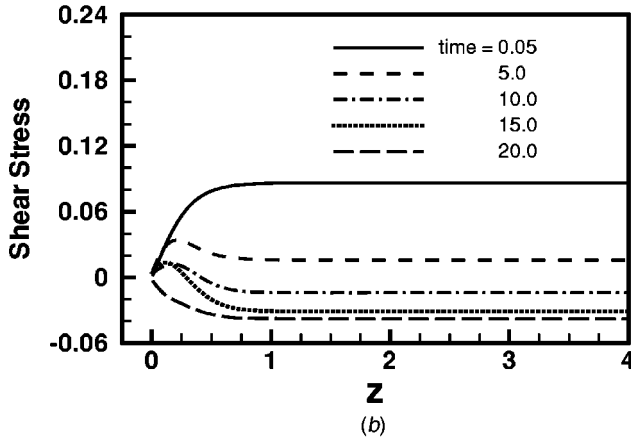
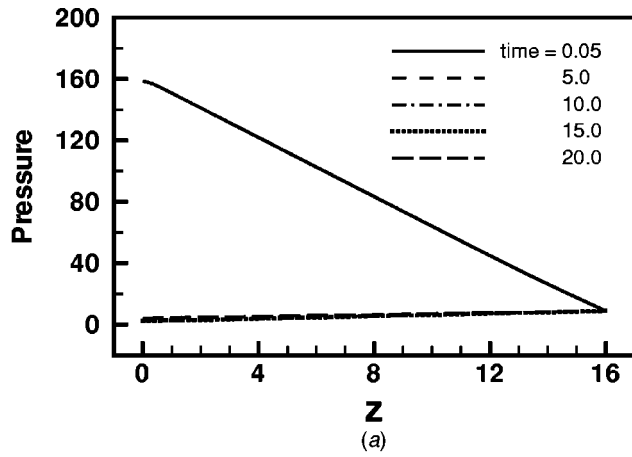


**Fig. 11 (a) Pressure and (b) shear stress along the top wall of the tube at various times for case 2 in Table 1,  $Re=106.90$ ,  $We=6.93$ ,  $St=10.47$ ,  $P_h=176.39$  ( $P_h^*=20$  bar),  $d_i=0.1$ . The horizontal axis indicates axial position,  $z$ . Only the significant portion of the tube,  $z \leq 4$ , for shear stress is shown. The dimensional stress is  $11,338.8$  N/m<sup>2</sup> per dimensionless unit. (c) Bubble shapes at times presented in (a) and (b).**

The physical dimensions and scales underlying the dimensionless parameters are as follows. The tube diameter is  $36 \mu\text{m}$ , which is the length scale. The tube length is set to be 32 times of the diameter, i.e.,  $32 \times 36 \mu\text{m} = 1.152$  mm. The initial bubble diameters considered are 3.6, 10.8, 18.0, 25.2, and  $32.4 \mu\text{m}$ , corresponding to 10%, 30%, 50%, 70%, and 90% of the tube diameter, respectively. With chosen initial pressure of 10 or 20 bar, the velocity scale is 1.628 or 3.440 m/s. The time scale, ratio of the length and velocity scale, is  $10.5 \times 10^{-6}$  or  $22.1 \times 10^{-6}$  s.

The size of the computational domain is  $32 \times 1$ , with 1 being the tube diameter and 32 being the tube length. After a grid refine-

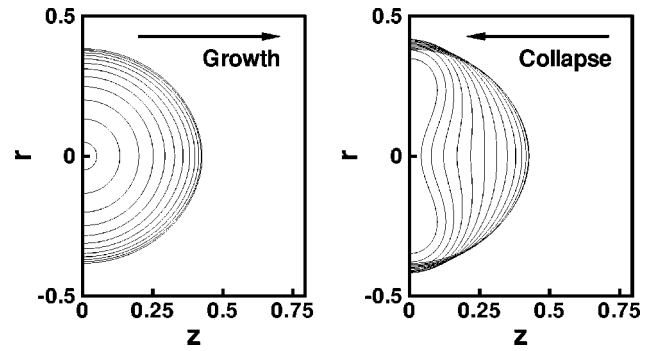


**Fig. 12 Bubble shapes at different times during growth (left graph) and collapse (right graph) for case 3 in Table 1,  $Re=427.59$ ,  $We=3.46$ ,  $St=10.47$ ,  $P_h=176.39$  ( $P_h^*=20$  bar),  $d_i=0.1$ . Only half of the bubble is shown because of symmetry. Time interval between successive shapes is 1 dimensionless unit ( $10.5 \times 10^{-6}$  s/unit). The computational domain extends to 16 in both directions on the  $z$  axis.**

ment study, a nonuniform, Cartesian grid of  $492 \times 52$  was chosen for the simulations. For a test case, the computed history of the bubble aspect ratio on this and a finer grid is plotted in Fig. 6. The two curves are almost identical, indicating that the grid  $492 \times 52$  has adequate spatial resolution. The bubble aspect ratio is defined as the ratio of the bubble diameter versus its length in the  $z$  direction. Both measures are on the major axes of the bubble.

**4.1 Effects of Viscosity, Surface Tension and Initial Pressure.** The results presented in this section correspond to an initial bubble diameter of 0.1, i.e., 10% of the tube diameter. That includes cases 1–4 in Table 1. In these cases, we examine the effects of changing viscosity, surface tension, as well as initial bubble pressure while keeping the initial bubble size fixed at 0.1. The Reynolds number ranges from 106.90 to 427.59, Weber number varies from 1.55 to 6.93, Strouhal number changes from 10.47 to 22.11, and initial bubble pressure is 10 or 20 bar.

Figure 7 shows the shape evolution of the bubble for case 1,  $Re=427.59$ ,  $We=6.93$ ,  $St=10.47$ ,  $P_h=176.39$  ( $P_h^*=20$  bar),  $d_i=0.1$ , at different time instants. Only half of the bubble ( $z > 0$ ) is shown owing to symmetry. The other half of the bubble on the negative  $z$  axis is the mirror image of that in the graph. The tube extends to  $\pm 16$  in the  $z$  direction.

Our primary goal in this study is to predict the stress exerted on the tube wall during bubble expansion and collapse processes. The stress profiles are shown in Fig. 8 for this case. The symbol N/m<sup>2</sup> in the figure denotes the ISO unit of stress, Newton per square meter, and the dimensional stress corresponding to a dimensionless stress of one is indicated. From the results, the pressure dominates the normal stress on the wall while the liquid viscous stress contribution to the normal stress is negligible. Figure 8(a) shows the pressure along the top wall of the tube at various times. The horizontal axis is the axial position along the tube from 0 to 16. The center of the bubble is at  $z=0$ . It is evident that, at the onset of the bubble growth driven by a high internal pressure, the wall pressure exhibits a linear variation from  $z=0$  to  $z=16$ , the exit of the tube. At later times, the wall pressure is much lower as liquid pressure becomes lower. This is typical for an inertia-driven process. The most unfavorable pressure condition occurs at the very beginning of the bubble expansion. The wall shear stress versus  $z$  is plotted in Fig. 8(b) for the same times. For better resolution of the shear stress variation near the center of the tube, only a portion of the tube,  $z \leq 4$ , is shown. The straight lines in the graph extend all the way to the tube exit at  $z=16$ . The uniformity of the shear stress along the majority of the tube is a result of the bulk flow in the tube, which indicates a nearly constant velocity away from the

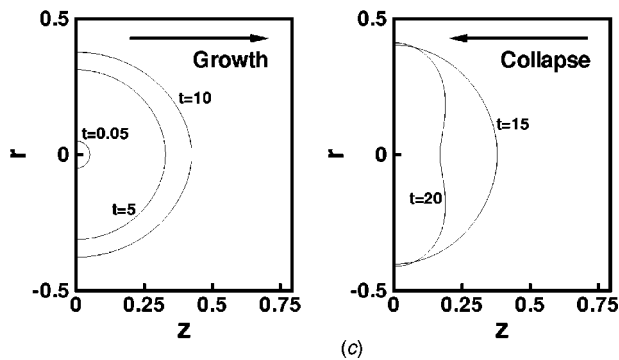
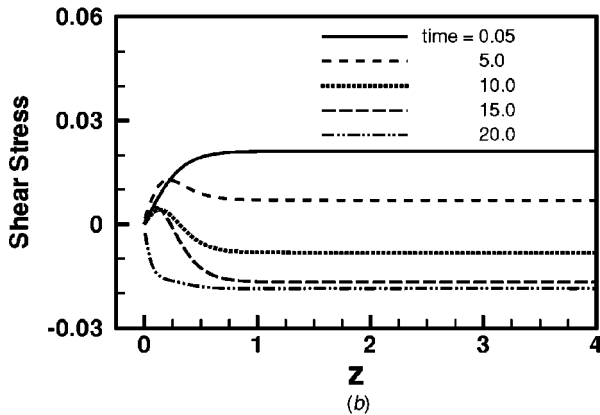
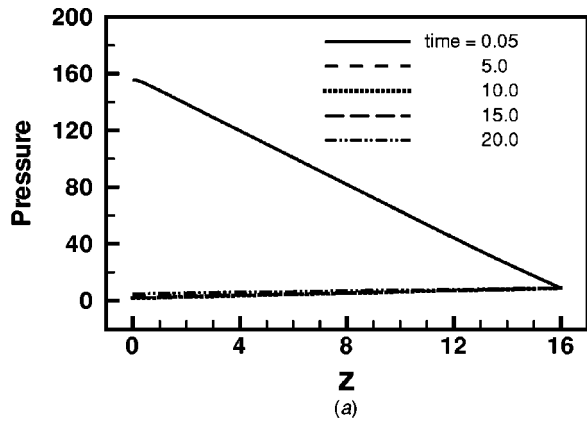


Fig. 13 (a) Pressure and (b) shear stress along the top wall of the tube at various times for case 3 in Table 1,  $Re=427.59$ ,  $We=3.46$ ,  $St=10.47$ ,  $P_h=176.39$  ( $P_h^*=20$  bar),  $d_i=0.1$ . The horizontal axis indicates axial position,  $z$ . Only the significant portion of the tube,  $z \leq 4$ , for shear stress is shown. The dimensional stress is  $11,338.8$  N/m<sup>2</sup> per dimensionless unit. (c) Bubble shapes at times presented in (a) and (b).

center of the tube. At  $z=0$ , the bulk motion in the horizontal direction is very small. The bubble size effect is not significant in the shear stress profile. Before the bubble switches from growth to collapse, the shear stress reverses its direction at  $t=10.0$ . This indicates a recirculation region has formed between the wall and the core flow in the tube, as seen in Fig. 9. During collapse, the shear stress is in the opposite direction and reaches roughly the same peak magnitude as in the growth stage. In general, the shear stress is much smaller than the pressure in magnitude. Figure 8(c) shows the bubble shapes at times corresponding to those in Figs. 8(a) and (b).

Similar illustrations for case 2,  $Re=106.90$ ,  $We=6.93$ ,  $St=10.47$ ,  $P_h=176.39$ ,  $d_i=0.1$ , are plotted in Figs. 10 and 11. In this case, the liquid viscosity is higher compared to case 1, reflected by a lower Reynolds number, 106.90. The maximum vol-

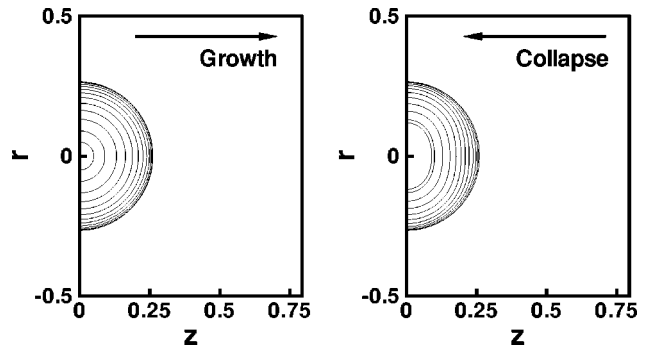


Fig. 14 Bubble shapes at different times during growth (left graph) and collapse (right graph) for case 4 in Table 1,  $Re=202.39$ ,  $We=1.55$ ,  $St=22.11$ ,  $P_h=393.66$  ( $P_h^*=10$  bar),  $d_i=0.1$ . Only half of the bubble is shown because of symmetry. Time interval between successive shapes is  $0.6$  dimensionless unit ( $22.1 \times 10^{-6}$  s/unit). The computational domain extends to  $16$  in both directions on the  $z$  axis.

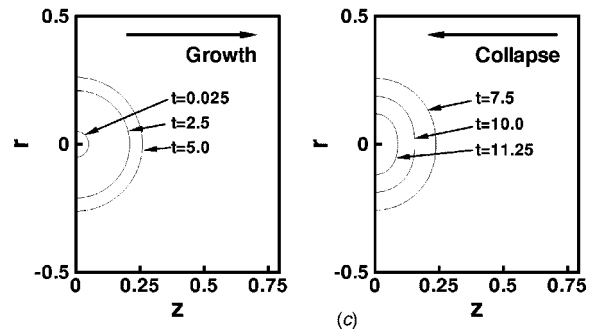
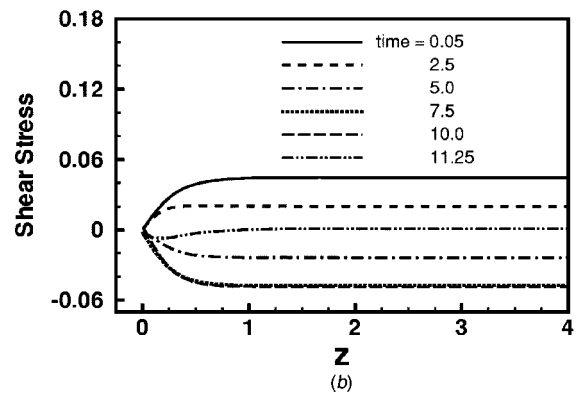
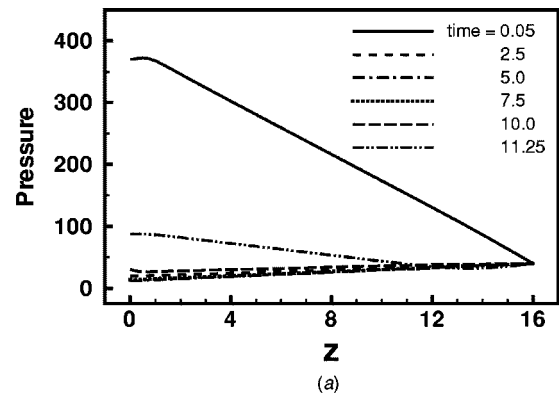


Fig. 15 (a) Pressure and (b) shear stress along the top wall of the tube at various times for case 4 in Table 1,  $Re=202.39$ ,  $We=1.55$ ,  $St=22.11$ ,  $P_h=393.66$  ( $P_h^*=10$  bar),  $d_i=0.1$ . The horizontal axis indicates axial position,  $z$ . Only the significant portion of the tube,  $z \leq 4$ , for shear stress is shown. The dimensional stress is  $2540.3$  N/m<sup>2</sup> per dimensionless unit. (c) Bubble shapes at times presented in (a) and (b).

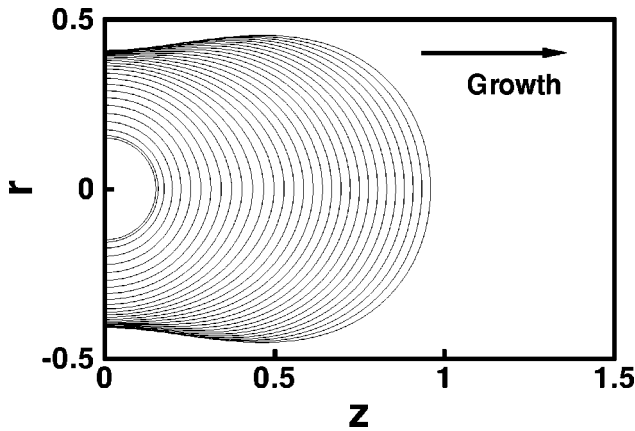


Fig. 16 Bubble shapes at different times for case 1-1 in Table 1,  $Re=427.59$ ,  $We=6.93$ ,  $St=10.47$ ,  $P_h=176.39$  ( $P_h^*=20$  bar),  $d_i=0.3$ . The initial bubble diameter is 0.3. Only half of the bubble is shown because of symmetry. Time interval between successive shapes is 0.25 dimensionless unit ( $10.5 \times 10^{-6}$  s/unit). The computational domain extends to 16 in both directions on the z axis.

ume of the bubble is smaller than that in case 1 (see Fig. 7). Additionally, the last bubble shape in the collapse graph does not extend as close to the wall as it does in case 1. These differences result from the higher liquid viscosity.

The wall pressure and shear stress of case 2 are similar to case 1. The maximum pressure occurs at the beginning. The peak magnitude of the shear stress is higher than that of case 1 due to the higher liquid viscosity. The higher surface tension of case 3, compared to that of case 1, gives rise to the shape evolution of Fig. 12. The dimensionless parameters in this case are  $Re=427.59$ ,  $We=3.46$ ,  $St=10.47$ ,  $P_h=176.39$ ,  $d_i=0.1$ . The pressure and the shear stress in Fig. 13 show similar profiles to those of case 1.

In case 4, we specify a lower initial bubble pressure, 10 bar, instead of 20 bar. The corresponding dimensionless parameters are  $Re=202.39$ ,  $We=1.55$ ,  $St=22.11$ ,  $P_h=393.66$ ,  $d_i=0.1$ . The lower initial pressure results in a much smaller maximum bubble volume when the bubble expands. Since the expansion process does not produce as much inertial energy in the liquid as in the previous cases, the bubble experiences much less deformation in the subsequent collapse process (see Fig. 14). This leads to multiple growth-collapse cycles. Largely through the liquid friction, the inertial energy of the high pressure is dissipated in the process. Eventually, the cyclic process stops and the bubble reaches an equilibrium state. The corresponding wall stress conditions within one growth-collapse cycle are plotted in Fig. 15. The pressure follows a similar pattern to other cases, and achieves its maximum magnitude at the very beginning of the process. The growth and collapse of the first cycle cause higher wall shear stresses than do subsequent bubble growth and collapse cycles, simply because the kinetic energy decreases with each cycle. The time variation of the shear stress also provides an indication of when the bulk flow in the tube reaches its highest velocity.

We note that the bubble does not break up during the collapse phase as has been observed for cavitation bubbles near planar walls [34,35]. Unlike in cavitation, the gas bubble in this work is superheated at ambient conditions, and thus does not completely collapse. The bubble apparently does not become small enough that bubble pressures are sufficient to induce breakup. In an experimental investigation of the use of bubble growth and collapse in an expanding tube for pumping [36], bubble breakup was not reported during either growth or collapse, and was not apparent in the bubble images.

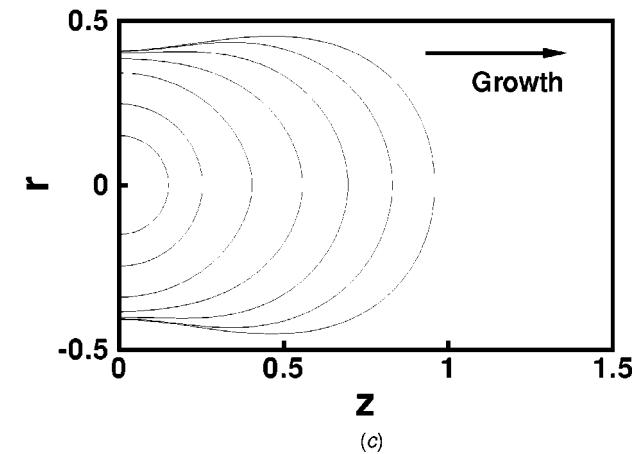
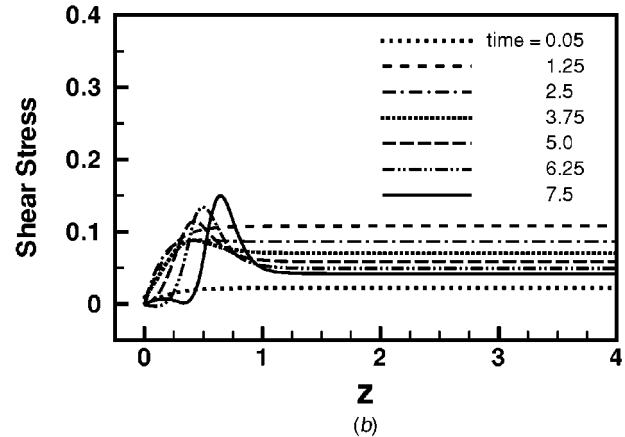
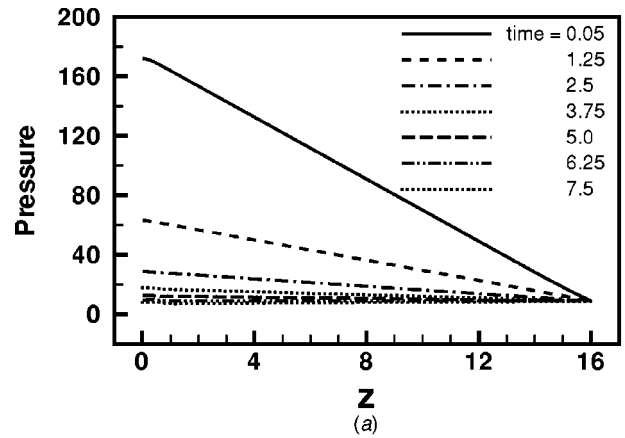
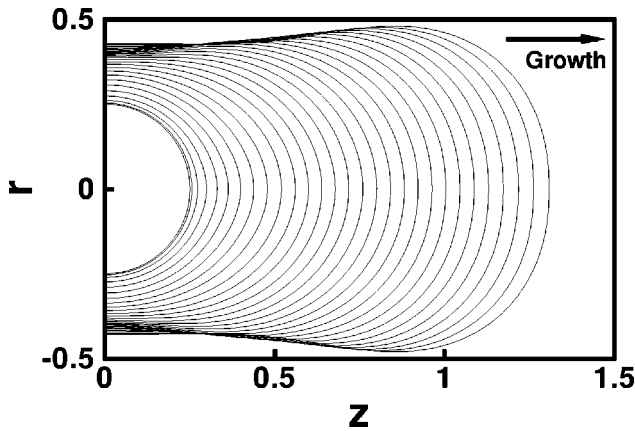


Fig. 17 (a) Pressure and (b) shear stress along the top wall of the tube at various times for case 1-1 in Table 1,  $Re=427.59$ ,  $We=6.93$ ,  $St=10.47$ ,  $P_h=176.39$  ( $P_h^*=20$  bar),  $d_i=0.3$ . The horizontal axis indicates axial position,  $z$ . Only the significant portion of the tube,  $z \leq 4$ , for shear stress is shown. The dimensional stress is  $11,338.8$  N/m<sup>2</sup> per dimensionless unit. (c) Bubble shapes at times presented in (a) and (b).

**4.2 Effect of Initial Bubble Size.** The results in this section demonstrate the effect of initial bubble size. Here, all dimensionless parameters are identical to those in case 1, i.e.,  $Re=427.59$ ,  $We=6.93$ ,  $St=10.47$ ,  $P_h=176.39$ , except the initial bubble size,  $d_i$ , which ranges from 0.3 to 0.9. For larger initial bubble diameters, the bubble interface moves closer to the tube wall during expansion than for the smaller initial bubble diameters. This results in higher local shear stress in the liquid region between the bubble and the tube. The simulations were terminated if the



**Fig. 18** Bubble shapes at different times for case 1-2 in Table 1,  $Re=427.59$ ,  $We=6.93$ ,  $St=10.47$ ,  $P_h=176.39$  ( $P_h^*=20$  bar),  $d_i=0.5$ . The initial bubble diameter is 0.5. Only half of the bubble is shown because of symmetry. Time interval between successive shapes is 0.25 dimensionless unit ( $10.5 \times 10^{-6}$  s/unit). The computational domain extends to 16 in both directions on the  $z$  axis.

bubble interface became too close to the wall. A wall adhesion model is needed to guide the subsequent evolution of the bubble. The results from expansion only provide adequate information about the maximum wall stresses since these occur early in the expansion phase.

Figures 16 and 17 show the interface shape and the wall stresses, respectively, for an initial bubble diameter of  $d_i=0.3$ . The pressure is high initially and then decreases (Fig. 17(a)). From Fig. 17(b), The shear stress increases to a maximum at  $t=1.25$ , and drops after  $t=1.25$ . Since the bulk shear stress is proportional to the bulk flow in the tube, this indicates that the peak velocity of the bulk flow is reached before  $t=1.25$ . The local shear stress maximum moves to the right in Fig. 17(b) as time progresses, and its location corresponds to where the bubble interface is closest to the tube wall as shown in Fig. 17(c). The maximum shear stress rises as time progresses due to the bubble interface moving closer to the tube wall. The shear stress is positive at all  $z$  locations during the growth process, indicating that a recirculation region has not yet formed near the wall.

For an initial bubble diameter of 0.5, the observed behavior is similar to that observed for an initial bubble diameter of 0.3 (see Figs. 18 and 19). The peak velocity of the bulk flow is reached before  $t=1.25$  as in Fig. 19(b). The brief negative shear stress near  $z=0.75$  at  $t=6.25$  (solid line) indicates there is a recirculation region between the bubble surface and the tube wall. It is also noted that as the bubble moves closer to the tube wall, the midpoint ( $z=0$ ) of the bubble is pushed inward, a result of the larger static pressure of the liquid at  $z=0$ . Thus the distance between the bubble interface and the tube wall is not uniform from the mid-point,  $z=0$ , towards the bubble tip. Computational studies using the boundary element method have also captured this dimpling behavior for a viscous droplet approaching a planar boundary in Stokes flow [55].

Pressure versus  $z$ , shear stress versus  $z$ , and the corresponding interface shapes are plotted at several times for an initial bubble diameter of 0.7 in Fig. 20. Interface shapes at later times are shown in Fig. 21. Figures 22 and 23 contain plots analogous to those in Figs. 20 and 21, respectively, for initial bubble diameter of 0.9. The peak velocity of the bulk flow for the bubble with initial diameter of 0.7 occurs between  $t=1.25$  and  $t=2.5$  judging from the shear stress plot (Fig. 21(b)) since the wall shear stress is proportional to the bulk flow velocity. For the bubble with initial diameter of 0.9, this peak velocity occurs between  $t=2.5$  and  $t$

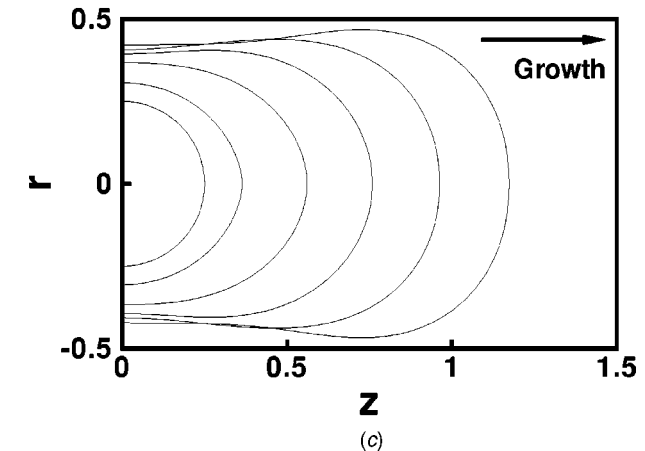
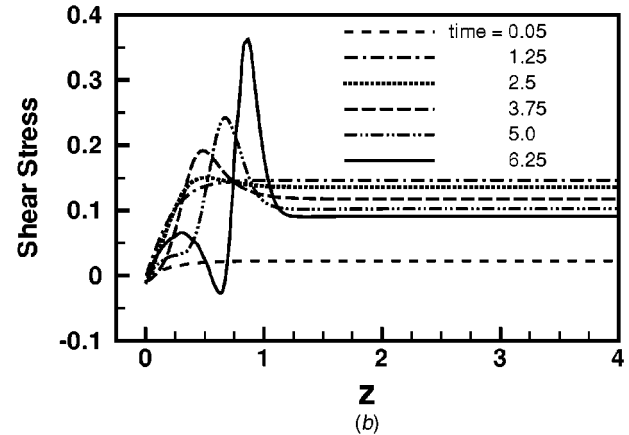
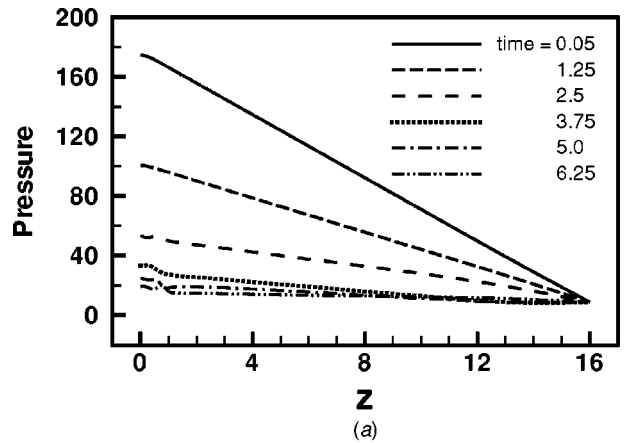


**Fig. 19** (a) Pressure and (b) shear stress along the top wall of the tube at various times for case 1-2 in Table 1,  $Re=427.59$ ,  $We=6.93$ ,  $St=10.47$ ,  $P_h=176.39$  ( $P_h^*=20$  bar),  $d_i=0.5$ . The horizontal axis indicates axial position,  $z$ . Only the significant portion of the tube,  $z \leq 4$ , for shear stress is shown. The dimensional stress is  $11,338.8$  N/m<sup>2</sup> per dimensionless unit. (c) Bubble shapes at times presented in (a) and (b).

$=3.75$  (Fig. 23(b)). It appears that the time required to achieve the peak velocity of the bulk flow is increased as the bubble size increases.

For initial bubble diameters greater than 0.1 (cases 1-1, 1-2, 1-3 and 1-4), we observed that interfaces become saddle shaped near  $z=0$ . As the bubble expands toward the tube wall, the liquid in between the wall and the bubble is squeezed out in both directions, resulting in nonzero velocity at  $z>0$  and  $z<0$ . Because of symmetry, the horizontal fluid velocity at  $z=0$  is zero. Analyzed

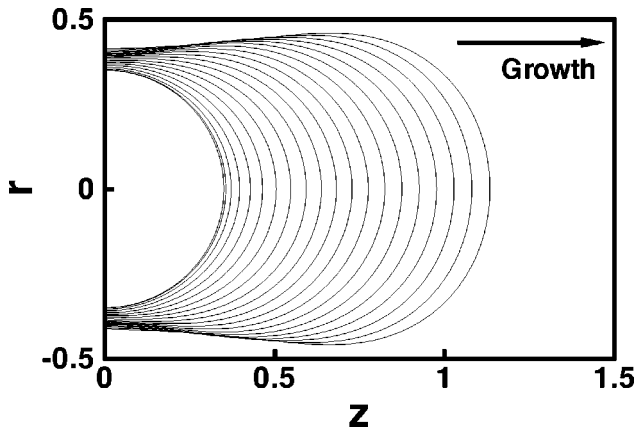


Fig. 20 Bubble shapes at different times for case 1-3 in Table 1,  $Re=427.59$ ,  $We=6.93$ ,  $St=10.47$ ,  $P_h=176.39$  ( $P_h^*=20$  bar),  $d_i=0.7$ . The initial bubble diameter is 0.7. Only half of the bubble is shown because of symmetry. Time interval between successive shapes is 0.25 dimensionless unit ( $10.5 \times 10^{-6}$  s/unit). The computational domain extends to 16 in both directions on the  $z$  axis.

by an approximation of the Bernoulli principle, the liquid static pressure along the thin film region enclosed by the tube wall and the bubble surface has a local maximum at  $z=0$ . The variation of net force along the bubble surface near  $z=0$  is dominated by the difference in the liquid static pressure because the bubble internal pressure is uniform and its surface tension is constant. Governed by the normal stress interfacial condition, the bubble interface yields to the larger liquid static pressure at  $z=0$ , resulting in the saddle shape. However, this behavior is largely missing in results from other studies on bubble expansion. As noted earlier, the continuous interface treatment of the single-domain numerical method often implemented for interfacial flows tends to smooth out the gradient of the pressure across the interface.

The pressure versus  $z$  and shear stress versus  $z$  are shown in Fig. 24 at  $t=2.5$  for a variety of initial bubble diameters. The influence of the initial bubble size on pressure and shear stress at the wall is significant, with larger  $d_i$  leading to higher wall stresses.

**4.3 Implication for Embolotherapy and Model Limitations.** The simulation results indicate that, for a given initial bubble size, the maximum pressure at the tube wall increases with the initial bubble pressure, and that the maximum occurs early in the bubble expansion. The vessel wall is therefore exposed to the highest risk of rupture at the beginning of the bubble expansion. The initial bubble size has a more significant effect on shear stress than do the other parameters. To minimize the potential of damaging the endothelium, smaller bubbles relative to the diameter of the blood vessel are favored. The overall magnitude of the shear stress is much less than that of the pressure.

Although the qualitative information obtained from simulation is valuable for the application of the embolotherapy, the quantitative relevance of the simulation results is dictated by the specified initial bubble pressure, and perhaps other modeling parameters as well. Specifying a uniform initial bubble pressure is an approximation of several concurrent dynamic and thermal physical mechanisms in the ADV process. There is no direct correspondence between this initial bubble pressure and a readily measured physical quantity.

Nonetheless, such a modeling quantity could be determined indirectly from an experiment. A proposed experimental plan is to conduct an experiment with a set of parameters that are identical to the simulations except for the initial bubble pressure. In the simulation, we can vary the initial bubble pressure while not

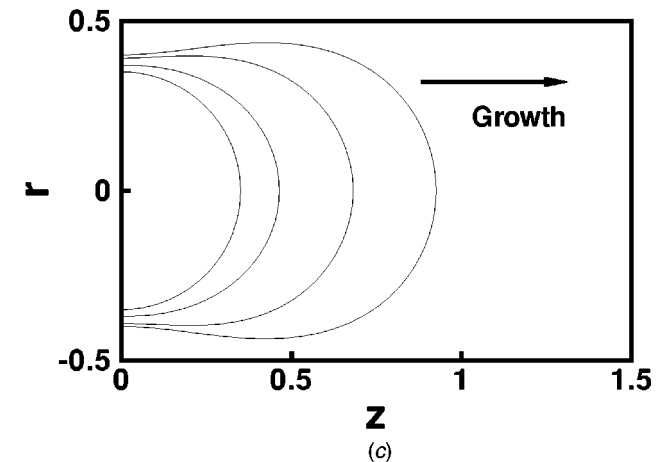
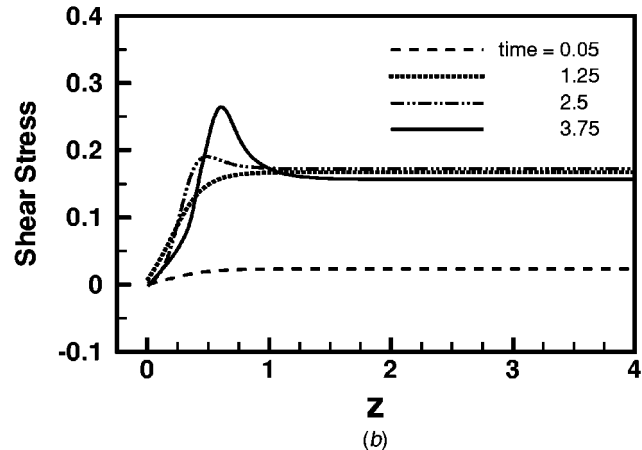
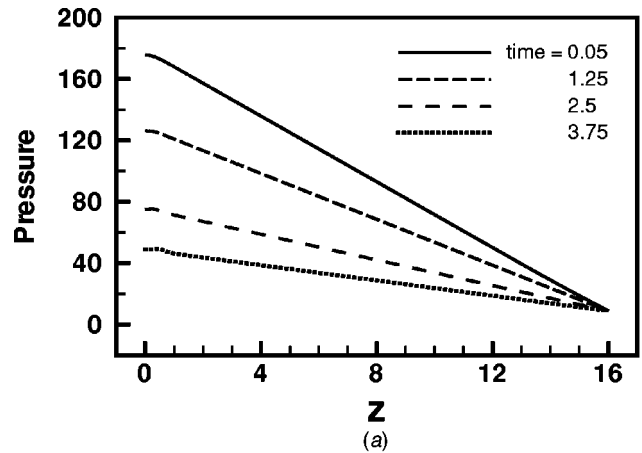
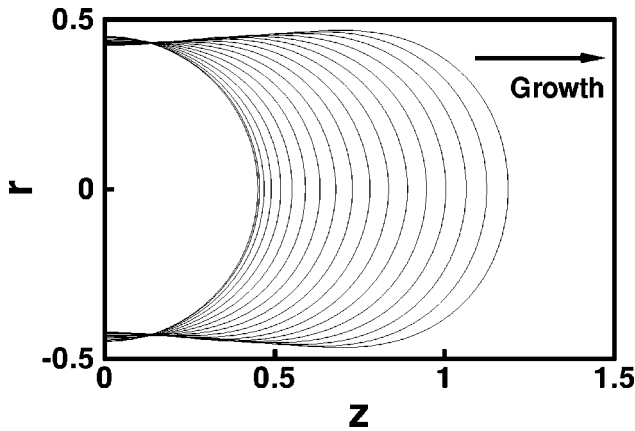


Fig. 21 (a) Pressure and (b) shear stress along the top wall of the tube at various times for case 1-3 in Table 1,  $Re=427.59$ ,  $We=6.93$ ,  $St=10.47$ ,  $P_h=176.39$  ( $P_h^*=20$  bar),  $d_i=0.7$ . The horizontal axis indicates axial position,  $z$ . Only the significant portion of the tube,  $z \leq 4$ , for shear stress is shown. The dimensional stress is  $11,338.8$  N/m<sup>2</sup> per dimensionless unit. (c) Bubble shapes at times presented in (a) and (b).

changing the other parameters. By testing different initial bubble pressures until a match of the terminal size of the bubble from experiment and simulation is found, the initial bubble pressure could be determined. This process may be regarded as a calibration of the simulation. For other settings, the corresponding initial pressure could be estimated by comparing all parameters with the



**Fig. 22** Bubble shapes at different times for case 1-4 in Table 1,  $Re=427.59$ ,  $We=6.93$ ,  $St=10.47$ ,  $P_h=176.39$  ( $P_h^*=20$  bar),  $d_i=0.9$ . The initial bubble diameter is 0.9. Only half of the bubble is shown because of symmetry. Time interval between successive shapes is 0.25 dimensionless unit ( $10.5 \times 10^{-6}$  s/unit). The computational domain extends to 16 in both directions on the  $z$  axis.

calibration experiment. The initial pressure would likely be a function of thermodynamic state whose parameters are measurable quantities.

A future improvement might be a molecular dynamics simulation with multiple time and length scales, combined with the present continuum simulation. Based on first principles using molecular dynamics simulations, the phase change and thermodynamic states of ADV at a very early stage could potentially be determined to serve as inputs for the current continuum simulations, eliminating the initial bubble pressure modeling. However, molecular dynamics simulations of phase transformations in relatively large spatial and temporal ranges demand extreme computational power and currently are under investigation in the research community.

In addition to the need for calibration of the initial bubble pressure, there are several other limitations of the current model. Foremost, the blood vessel wall is mechanically compliant, and can adapt itself to the blood flow rate or pressure. This physical feature is expected to significantly alter the wall stress. A flexible wall enhancement is our priority in further investigations of bubble-fluid-structure interaction. When the wall is flexible, part of the energy from the bubble pressure will be absorbed by the deformation of the vessel wall due to the increased liquid pressure during the bubble expansion.

The vasculature is a closed, branching tube network, and the pressure in the blood vessel is, in general, pulsatile. In this study, the blood vessel is modeled as an open-ended, albeit long, tube connecting two reservoirs, each with the same constant pressure. The length of the tube and the ambient pressure condition are expected to affect the magnitude and the time phase of the peak forces on the tube wall. Examining different lengths and ambient pressure conditions represents a next step in developing this model.

## 5 Summary

A computational model is presented to study unsteady, micro-scale bubble dynamics in a tube in order to assess the risk of vessel damage during a potential gas embolotherapy technique. The model consists of a bubble inside a long tube open to liquid reservoirs. A moving interface separates a viscous, incompressible liquid from an ideal gas. The effects of dimensionless parameters Reynolds, Weber and Strouhal numbers, as well as initial bubble pressure and size, were investigated. Since the wall stresses are

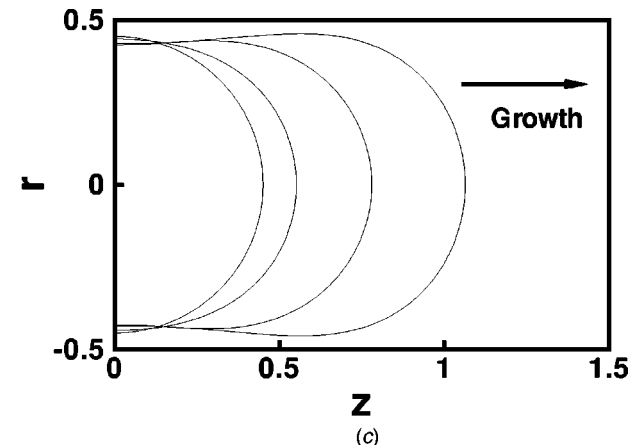
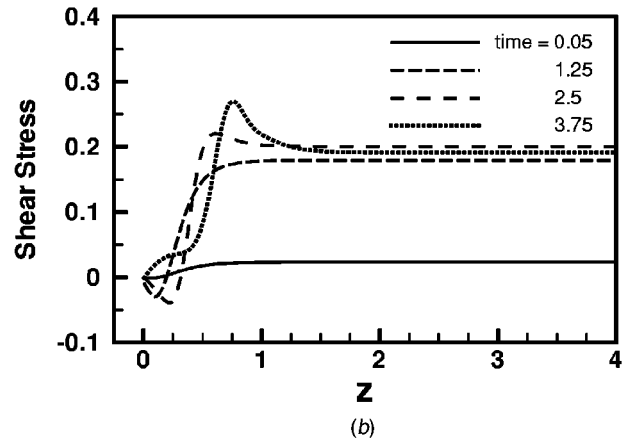
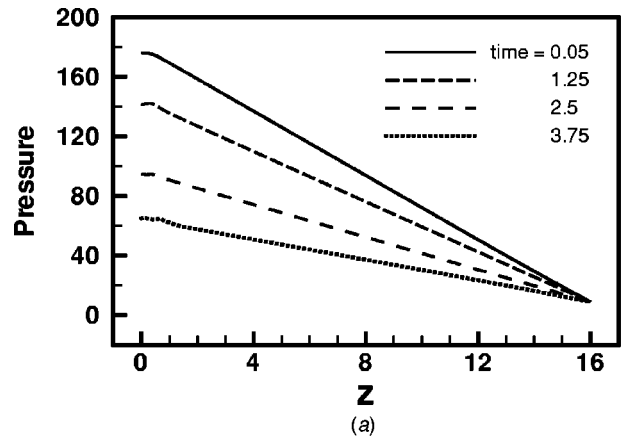


**Fig. 23** (a) Pressure and (b) shear stress on the top wall of the tube at various times for case 1-4 in Table 1,  $Re=427.59$ ,  $We=6.93$ ,  $St=10.47$ ,  $P_h=176.39$  ( $P_h^*=20$  bar),  $d_i=0.9$ . The horizontal axis indicates axial position,  $z$ . Only the significant portion of the tube for shear stress is shown. The stress is  $11,338.8$  N/m<sup>2</sup> per dimensionless unit. (c) Bubble shapes at times presented in (a) and (b).

determined by localized, small-scale fluid dynamics, a multi-domain, sharp-interface, moving boundary method is employed.

For this and similar problems involving a bubble in a tube, this report is the first systematic presentation of the stress conditions on the tube wall for a range of dimensionless parameters. The normal wall stress is dominated by pressure while the viscous component of the normal stress is negligible. The wall pressure typically reaches a maximum at an early time during the expansion process, and quickly returns to the ambient level. The maxi-

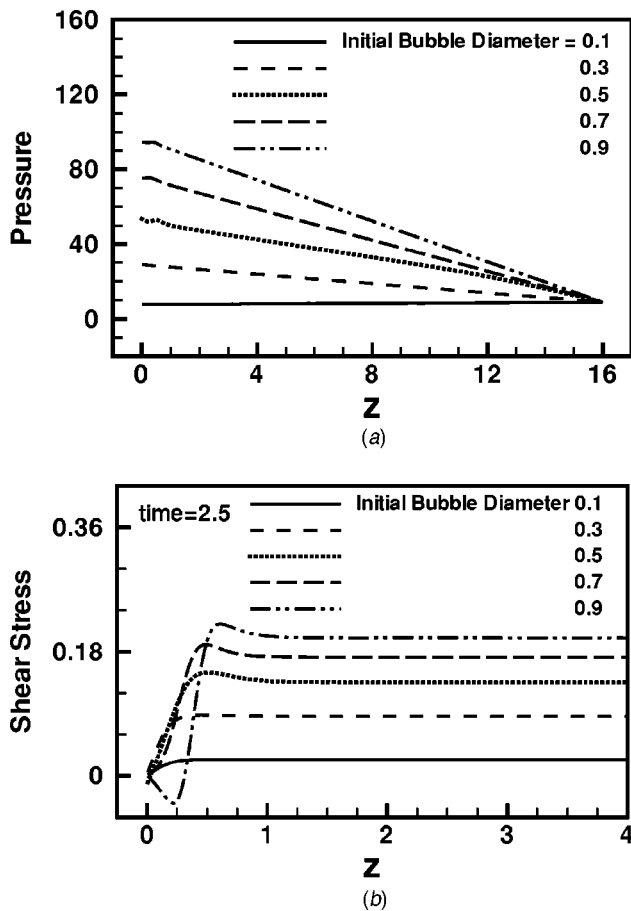


**Fig. 24 (a) Pressure and (b) shear stress on the top wall of the tube for varying initial bubble diameters,  $d_i$ , while all other dimensionless parameters being fixed,  $Re=427.59$ ,  $We=6.93$ ,  $St=10.47$ ,  $P_h=176.39$  ( $P_h^*=20$  bar). The results at  $t=2.5$  since onset of the bubble expansion are shown.**

imum wall pressure depends weakly on the initial bubble size, and strongly on the initial bubble pressure. Although lower in magnitude than the pressure on the tube wall, the wall shear stress has a strong dependence on the initial bubble size and local flow features, e.g., recirculation. Higher initial bubble volumes lead to higher values of wall shear stress. In order to reduce the likelihood of endothelium damage due to the shear stress, smaller initial bubble diameters relative to the tube diameter, and lower liquid density to vapor density ratios, are preferred.

### Acknowledgments

This work was supported by NIH Grant No. EB003541-01 and NSF Grant No. BES-0301278. Computational resources were provided by the National Computational Science Alliance under BIO030007N utilizing an IBM P690 parallel computer. The authors thank Dr. J. Brian Fowlkes and Dr. Oliver D. Kripfgans for valuable discussions.

### References

[1] Di Segni, R., Young, A. T., Zhong, Q., and Castaneda-Zuniga, W. R., 1997, "Embolotherapy: Agents, Equipment, and Techniques," in *Interventional Radiology*, W. R. Castaneda-Zuniga, ed., Williams and Wilkins, Baltimore, pp. 81–84.  
 [2] Lussenhop, A. J., and Spence, W. T., 1960, "Artificial Embolization of Cerebral Arteries: Report of Use in a Case of Arteriovenous Malformation," *JAMA, J. Am. Med. Assoc.*, **172**, pp. 1153–1155.  
 [3] Serbinenko, F., 1974, *Balloon Occlusion of Saccular Aneurysms of the Cerebral Arteries*. Voprosy Neurokhirurgii.

[4] Boehm, T., Folkman, J., Browder, T., and O'Reilly, M. S., 1997, "Antiangiogenic Therapy of Experimental Cancer Does Not Induce Acquired Drug Resistance," *Nature (London)*, **390**, pp. 404–407.  
 [5] Laccourreye, O., Laurent, A., Polivka, M., Wassef, M., Domas, L., Grasnu, D., and Merland, J., 1993, "Biodegradable Starch Microspheres for Cerebral Arterial Embolization," *Invest. Radiol.*, **28**, pp. 150–154.  
 [6] Nakagawa, N., and Castaneda-Zuniga, W. R., 1997, "Transcatheter Chemoembolization for Hepatocellular Carcinoma and Other Promising Transarterial Therapies," in *Interventional Radiology*, W. R. Castaneda-Zuniga, ed., Williams and Wilkins, Baltimore.  
 [7] Kripfgans, O. D., Fowlkes, J. B., Woydt, M., Eldevik, O. P., and Carson, P. L., 2002, "In Vivo Droplet Vaporization for Occlusion Therapy and Phase Aberration Correction," *IEEE Trans. Ultrason. Ferroelectr. Freq. Control*, **49**, pp. 726–738.  
 [8] Kripfgans, O. D., Fowlkes, J. B., Miller, D. L., Eldevik, O. P., and Carson, P. L., 2000, "Acoustic Droplet Vaporization for Therapeutic and Diagnostic Applications," *Ultrasound Med. Biol.*, **26**(7), pp. 1177–1189.  
 [9] Linka, A. Z., Skalak, T. C., Skyba, D. M., Price, R. J., and Kaul, S., 1998, "Direct in Vivo Visualization of Intravascular Destruction of Microbubbles by Ultrasound and Its Local Effects on Tissue," *Circulation*, **98**, pp. 290–293.  
 [10] Qi, M., VanGieson, E. J., Kaul, S., Song, J., Chappell, J. C., and Price, R. J., 2002, "Influence of Injection Site, Microvascular Pressure and Ultrasound Variables on Microbubble-Mediated Delivery of Microspheres to Muscle," *J. Am. Coll. Cardiol.*, **39**, pp. 726–731.  
 [11] Van Camp, G., Campanelli, B., Gisellu, G., Pasquet, A., Deneff, J. F., Melin, J. A., Ay, T., Havaux, X., and Vanocershelde, J. L. J., 2001, "Destruction of Contrast Microbubbles by Ultrasound-Effects on Myocardial Function, Coronary Perfusion Pressure, and Microvascular Integrity," *Circulation*, **104**, pp. 461–466.  
 [12] Miller, D. L., and Qudus, J., 2000, "Diagnostic Ultrasound Activation of Contrast Agent Gas Bodies Induces Capillary Rupture in Mice," *Proc. Natl. Acad. Sci. U.S.A.*, **97**, pp. 10179–10184.  
 [13] Kaul, S., Song, J., Qi, M., and Price, R. J., 2002, "Stimulation of Arteriogenesis in Skeletal Muscle by Microbubble Destruction With Ultrasound," *Circulation*, **106**, pp. 1550–1555.  
 [14] Lelkes, P. I., 1999, *Mechanical Forces and the Endothelium*, Harwood, Amsterdam.  
 [15] Cornhill, J. F., Levesque, M. J., Herderick, E. E., Nerem, R. M., Kilman, J. W., and Vasko, J. S., 1980, "Quantitative Study of the Rabbit Aortic Endothelium Using Vascular Casts," *Atherosclerosis*, **35**, pp. 321–337.  
 [16] Dewey, Jr., C. F., Bussolari, S. R., Gimbrone, Jr., M. A., and Davies, P. F., 1981, "The Dynamic Response of Vascular Endothelial Cells to Fluid Shear Stress," *ASME J. Biomech. Eng.*, **103**, pp. 177–185.  
 [17] Nerem, R. M., Levesque, M. J., and Cornhill, J. F., 1981, "Vascular Endothelial Morphology as an Indicator of Blood Flow," *ASME J. Biomech. Eng.*, **103**, pp. 172–176.  
 [18] Levesque, M. J., and Nerem, R. M., 1985, "The Elongation and Orientation of Cultured Endothelial Cells in Response to Shear Stress," *ASME J. Biomech. Eng.*, **107**, pp. 341–347.  
 [19] Nerem, R. M., 1992, "Vascular Fluid Mechanics, the Arterial Wall, and Atherosclerosis," *ASME J. Biomech. Eng.*, **114**, pp. 274–282.  
 [20] Nerem, R. M., Harrison, D. G., Taylor, W. R., and Alexander, R. W., 1993, "Hemodynamics and Vascular Endothelial Biology," *J. Cardiovasc. Pharmacol.*, **21**, pp. 6–10.  
 [21] Franke, R. P., Grafe, M., Schnittler, H., Seiffge, D., Mittermayer, C., and Drenckhahn, D., 1984, "Induction of Human Vascular Endothelial Stress Fibers by Fluid Shear Stress," *Nature (London)*, **307**, pp. 648–649.  
 [22] Kim, D. W., Gotlieb, A. L., and Langille, B. L., 1989, "In Vivo Modulation of Endothelial f-Actin Microfilaments by Experimental Alterations in Shear Stress," *Atherosclerosis*, **9**, pp. 439–445.  
 [23] Ookawa, K., Sato, M., and Ohshima, N., 1992, "Changes in the Microstructure of Cultured Porcine Aortic Endothelial Cell in the Early Stage After Applying a Fluid-Imposed Shear Stress," *ASME J. Biomech. Eng.*, **114**, pp. 274–282.  
 [24] Olesen, S. P., Clapham, D. E., and Davies, P. F., 1988, "Hemodynamic Shear Stress Activates a k Current in Vascular Endothelial Cells," *Nature (London)*, **331**, pp. 168–170.  
 [25] Davies, P. F., Robotewskyj, A., Griem, M. L., Dull, R. O., and Polacek, D. C., 1992, "Hemodynamics Forces and Vascular Cell Communication in Arteries," *Arch. Pathol. Lab Med.*, **116**, pp. 1301–1306.  
 [26] Davies, P. F., and Tripathi, S. C., 1993, "Mechanical Stress Mechanisms and the Cell: an Endothelial Paradigm," *Circ. Res.*, **72**, pp. 239–245.  
 [27] Nollert, M. N., Diamond, S. L., and McIntire, L. V., 1991, "Hydrodynamic Shear Stress and Mass Transport Modulation of Endothelial Cell Metabolism," *Biotechnol. Bioeng.*, **38**, pp. 588–602.  
 [28] Shyy, Y. J., Hsieh, H. J., Usami, S., and Chien, S., 1994, "Fluid Shear Stress Induces a Biphasic Response of Human Monocyte Chemotactic Protein 1 Gene Expression in Vascular Endothelium," *Proc. Natl. Acad. Sci. U.S.A.*, **91**, pp. 4678–4682.  
 [29] Chiu, J. J., Wang, D. L., Chien, S., Skalak, R., and Usami, S., 1998, "Effects of Disturbed Flows on Endothelial Cells," *J. Biomech. Eng.*, **120**, pp. 2–8.  
 [30] Dayton, P. A., Morgan, K. E., Klibanov, A. L., Brandenburger, G. H., and Ferrara, K. W., 1999, "Optical and Acoustical Observations of the Effects of Ultrasound on Contrast Agents," *IEEE Trans. Ultrason. Ferroelectr. Freq. Control*, **46**(1), pp. 220–232.  
 [31] Patel, D., Dayton, P. A., Gut, J., Wisner, E., and Ferrara, K. W., 2002, "Optical

- and Acoustical Interrogation of Submicron Contrast Agents," IEEE Trans. Ultrason. Ferroelectr. Freq. Control, **49**(12), pp. 1641–1651.
- [32] Allen, J. S., Kruse, D. E., Dayton, P. A., and Ferrara, K. W., 2003, "Effect of Coupled Oscillations on Microbubble Behavior," J. Acoust. Soc. Am., **114**(3), pp. 1678–1690.
- [33] Bloch, S. H., Wan, M., Dayton, P. A., and Ferrara, K. W., 2004, "Optical Observation of Lipid- and Polymer-Shelled Ultrasound Microbubble Contrast Agents," Appl. Phys. Lett., **84**(4), pp. 631–633.
- [34] Brujan, E. A., Keen, G. S., Vogel, A., and Blake, J. R., 2002, "The Final Stage of the Collapse of a Cavitation Bubble Close to a Rigid Boundary," Phys. Fluids, **14**, pp. 85–92.
- [35] Tong, R. P., Schiffers, W. P., Shaw, S. J., Blake, J. R., and Emmony, D. C., 1999, "The Role of 'Splashing' in the Collapse of a Laser-Generated Cavity Near a Rigid Boundary," J. Fluid Mech., **380**, pp. 339–361.
- [36] Geng, X., Yuan, H., Oguz, H. N., and Prosperetti, A., 2001, "Bubble-Based Micropump for Electrically Conducting Liquids," J. Micromech. Microeng., **11**, pp. 270–276.
- [37] Ory, E., Yuan, H., Prosperetti, A., Popinet, S., and Zaleski, S., 2000, "Growth and Collapse of a Vapor Bubble in a Narrow Tube," Phys. Fluids, **12**, pp. 1268–1277.
- [38] Pozrikidis, C., 2001, "Interfacial Dynamics for Stokes Flow," J. Comput. Phys., **169**, pp. 250–301.
- [39] Power, H., and Wrobel, L. C., 1995, *Boundary Integral Methods in Fluid Mechanics*, Computational Mechanics Publications, Southampton, UK.
- [40] Kothe, D. B., and Mjolsness, R. C., 1992, "Ripple: A New Model for Incompressible Flows With Free Surfaces," AIAA J., **30**, pp. 2694–2700.
- [41] Unverdi, S. O., and Tryggvason, G., 1992, "A Front Tracking Method for Viscous Incompressible Flows," J. Comput. Phys., **100**, pp. 25–37.
- [42] Sussman, M., Smereka, P., and Osher, S., 1994, "A Level-Set Approach for Computing Solutions to Incompressible Two-Phase Flow," J. Comput. Phys., **114**, pp. 146–159.
- [43] Jacqmin, D., 1999, "Calculation of Two-Phase Navier-Stokes Flows Using Phase-Field Modeling," J. Comput. Phys., **155**, pp. 96–127.
- [44] Kang, M., Fedkiw, R. P., and Liu, X., 2000, "A Boundary Condition Capturing Method for Multiphase Incompressible Flow," J. Sci. Comput., **15**, pp. 323–360.
- [45] Brackbill, J. U., Kothe, D. B., and Zemach, C., 1992, "A Continuum Method for Modeling Surface Tension," J. Comput. Phys., **100**, pp. 335–354.
- [46] Williams, M. W., Kothe, D. B., and Puckett, E. G., 1999, "Accuracy and Convergence of Continuum Surface-Tension Models," in *Fluid Dynamics at Interfaces*, W. Shyy and W. Narayanan, eds., Cambridge University Press, New York.
- [47] Ye, T., Shyy, W., Tsai, P., and Chung, J. N., 2004, "Assessment of Sharp- and Continuous Interface Methods for Drop in Static Equilibrium," Comput. Fluids, **33**(7), pp. 917–926.
- [48] Ye, T., Mittal, R., Udaykumar, H. S., and Shyy, W., 1999, "An Accurate Cartesian Grid Method for Viscous Incompressible Flows With Complex Immersed Boundaries," J. Comput. Phys., **156**, pp. 209–240.
- [49] Ye, T., Shyy, W., and Chung, J. N., 2001, "A Fixed-Grid, Sharp-Interface Method for Bubble Dynamics and Phase Change," J. Comput. Phys., **174**, pp. 781–815.
- [50] Farin, G., 1997, *Curves and Surfaces for Computer-Aided Geometric Design, A Practical Guide*, 4th ed., Academic Press, San Diego.
- [51] Sapidis, N., and Farin, G., 1990, "Automatic Fairing Algorithm for b-Spline Curves," Comput.-Aided Des., **22**(2), pp. 121–129.
- [52] Chorin, A. J., 1968, "Numerical Solution of the Navier-Stokes Equations," Math. Comput., **22**, pp. 745–762.
- [53] Kim, J., and Moin, P., 1985, "Application of a Fractional Step Method to Incompressible Navier-Stokes Equations," J. Comput. Phys., **59**, pp. 308–323.
- [54] Zang, Y., Street, R. L., and Koseff, J. R., 1994, "A Non-Staggered Grid, Fractional Step Method for Time-Dependent Incompressible Navier-Stokes Equations in Curvilinear Coordinates," J. Comput. Phys., **114**, pp. 18–33.
- [55] Pozrikidis, C., 1990, "The Deformation of a Liquid Drop Moving Normal to a Plane Wall," J. Fluid Mech., **210**, pp. 331–363.